ORNL/TM-2022/2710

Gantryless Associated-Particle Neutron Radiography

Matthew R. Heath
Jake Daughhetee
Paul Hausladen
Jason Newby
James Matta

September 2022

**Approved for public release.
Distribution is unlimited.**

ORNL IS MANAGED BY UT-BATTELLE LLC FOR THE US DEPARTMENT OF ENERGY

DOCUMENT AVAILABILITY

Reports produced after January 1, 1996, are generally available free via OSTI.GOV.

Website www.osti.gov

Reports produced before January 1, 1996, may be purchased by members of the public from the following source:

National Technical Information Service
5285 Port Royal Road
Springfield, VA 22161
Telephone 703-605-6000 (1-800-553-6847)
TDD 703-487-4639
Fax 703-605-6900
E-mail info@ntis.gov
Website http://classic.ntis.gov/

Reports are available to US Department of Energy (DOE) employees, DOE contractors, Energy Technology Data Exchange representatives, and International Nuclear Information System representatives from the following source:

Office of Scientific and Technical Information
PO Box 62
Oak Ridge, TN 37831
Telephone 865-576-8401
Fax 865-576-5728
E-mail reports@osti.gov
Website https://www.osti.gov/

This report was prepared as an account of work sponsored by an agency of the United States Government. Neither the United States Government nor any agency thereof, nor any of their employees, makes any warranty, express or implied, or assumes any legal liability or responsibility for the accuracy, completeness, or usefulness of any information, apparatus, product, or process disclosed, or represents that its use would not infringe privately owned rights. Reference herein to any specific commercial product, process, or service by trade name, trademark, manufacturer, or otherwise, does not necessarily constitute or imply its endorsement, recommendation, or favoring by the United States Government or any agency thereof. The views and opinions of authors expressed herein do not necessarily state or reflect those of the United States Government or any agency thereof.

ORNL/TM-2022/2710

Physics Division

GANTRYLESS ASSOCIATED-PARTICLE NEUTRON RADIOGRAPHY

Matthew R. Heath
Jake Daughhetee
Paul Hausladen
Jason Newby
James Matta

September 2022

Prepared by
OAK RIDGE NATIONAL LABORATORY
Oak Ridge, TN 37831
managed by
UT-BATTELLE LLC
for the
US DEPARTMENT OF ENERGY
under contract DE-AC05-00OR22725

CONTENTS

LIST OF FIGURES v
LIST OF TABLES v
ABBREVIATIONS vii
ACKNOWLEDGEMENTS ix
ABSTRACT 1
1. INTRODUCTION 1
    1.1 THE API SYSTEM 2
2. DETECTOR CALIBRATIONS 4
    2.1 CALIBRATION MEASUREMENTS 4
    2.2 TIMING CALIBRATIONS 7
    2.3 DIRECTION CALIBRATIONS 10
        2.3.1 Simulations to Investigate Systematic Effects 12
3. DETECTOR LOCALIZATION 17
    3.1 POSITION INFERRENCE VIA COINCIDENCE DATA 17
    3.2 LOCALIZATION PERFORMANCE AND SENSITIVITY 20
4. VOIDLESS NORMALIZATION 21
    4.1 RELATIVE PIXEL EFFICIENCY NORMALIZATION 21
    4.2 ABSOLUTE PANEL EFFICIENCY 22
    4.3 ALPHA CONE PROJECTION 23
    4.4 APPLICATION TO DATA 25
        4.4.1 Void Dataset 25
        4.4.2 Object Dataset 27
5. IMAGE STITCHING 28
6. SUMMARY/CONCLUSIONS 31
7. REFERENCES 31

LIST OF FIGURES

Figure 1. Schematic of an exemplar system using the API technique. 2
Figure 2. Photographs of the alpha-particle detector during different stages of assembly. 3
Figure 3. The data acquisition enclosure. 3
Figure 4. The neutron detector panel. 4
Figure 5. Detector setup for calibration measurements. 5
Figure 6. Top-down view of a measurement schematic showing the coordinate system used to measure alpha-cone directions and evaluate the source-detector geometry. 7
Figure 7. Change in the measured TOF-subtracted time neutron-alpha time difference throughout a single iteration of the neutron/alpha-particle pixel timing calibrations. 9
Figure 8. Timing resolution of the 14.1 MeV neutron transmission peak as a function of the number of pixel timing calibration iterations..9
Figure 9. Neutron TOF-subtracted coincidence time spectra integrated over all neutron and alpha-particle pixels. 10
Figure 10. Example alpha-particle pixel neutron hit patterns. 11
Figure 11. Alpha-particle pixel-defined unit vector *x* and *y* components. 11
Figure 12. The 3D event display of the neutron panel Geant4 simulation geometry with four simulated 14.1 MeV neutron events. 12
Figure 13. Pixel hit map from the Geant4 simulation. 13
Figure 14, Comparison of calculated and true neutron-cone directions from simulated data. 15
Figure 15. Sensitivity to panel placement. 16
Figure 16. Difference in *x*- and *y*-components of the true and fit alpha-particle unit vectors as a function of the mean pixel row and column of the 2D Gaussian fit. 16
Figure 17. Difference between calculated and true neutron cone directions as a function of neutron incidence angle. 17
Figure 18. TOF spectrum for neutron events in pixel 448. 18
Figure 19. Map of coincident hits in alpha-particle pixel space for neutron pixel 448. 19
Figure 20. Relative neutron pixel efficiency correction to calculate the void-less normalization..............22
Figure 21. Absolute neutron panel detection efficiency. 23
Figure 22. Numerical integration of alpha-particle cone across the face of the neutron panel as a function of distance for a cone pointed at the center of the detector. 24
Figure 23. Voidless normalization. 25
Figure 24. Final normalization from a void dataset. 26
Figure 25. Object measurement to test voidless normalization calculation consisting of a steel ring and lead brick. 27
Figure 26. Final normalization from the steel ring and lead brick dataset...28
Figure 27. Illustration of three sequential neutron detector panel positions within the neutron coincident cone of the API D-T generator. 29
Figure 28. Set of radiographic images of the object in Figure 25 projected onto a common plane. 30
Figure 29. Composite radiograph formed by stitching multiple radiographic images. 30

LIST OF TABLES

Table 1. Calibration measurement geometries used to evaluate timing calibrations and alpha-pixel-defined neutron unit vectors 6
Table 2. Assumed true and reconstructed positions of the neutron panel using the localization routine 20
Table 3. Standard deviation of fit parameters for subsets of long-dwell data 20

ABBREVIATIONS

API	associated-particle imaging
D-T	deuterium–tritium
FWHM	full width at half maximum
LVDS	low-voltage differential signaling
ORNL	Oak Ridge National Laboratory
PMT	photomultiplier tube
PSD	pulse-shape discrimination
TOF	time of flight

ACKNOWLEDGEMENTS

This work is supported by the US Department of Energy, Office of Defense Nuclear Nonproliferation Research and Development in the National Nuclear Security Administration (NA-22).

ABSTRACT

The present work reports on the development of techniques for in-field fast-neutron radiography measurements using the associated-particle imaging (API) method. The API method employs alpha-neutron coincidences from the $d + t \rightarrow \alpha + n$ reaction to enable fast neutron transmission imaging with excellent contrast using a wide cone beam. However, for field radiography applications, the API method is burdened by the need for the relative positions of the source and detector to be known. Fortunately, these relative positions can be inferred from transmission data. The inferred positions also enable accurate stitching of multiple images into a composite image even when using a low-resolution detector panel and acquiring images that have few overlapping pixels. The developed techniques address analysis of measurements for which (1) the source and detector panel are separately hand positioned rather than held in registration by a gantry, (2) multiple detector panel positions within the coincident cone of tagged neutrons are required to piece together an image of an item of interest, and (3) it is not possible to obtain normalization measurements that have identical source–detector positioning but that do not include the inspected object. The present work describes the system calibrations—including timing calibrations and neutron direction calibrations—necessary for subsequent analyses, the method of locating the detector in the coincident cone of neutrons with millimeter precision using the timing and directions of coincident neutrons, the method of calculating a normalization image for a given detector panel position, and the method used to project multiple images into a common image.

1. INTRODUCTION

Over the past decade, the US Department of Energy's Oak Ridge National Laboratory (ORNL) developed 3D tomographic imaging techniques using fast neutrons produced via the $d + t \rightarrow \alpha + n$ reaction in deuterium–tritium (D-T) neutron generators. These techniques employed the API technique, in which the time and location of detected alpha particles, ascertained by a detector embedded in the D-T neutron generator, determine the time and direction of the associated 14.1 MeV neutrons. Earlier efforts concentrated on tomographic measurements using laboratory imaging systems. These systems employed gantries to position the source and detector with respect to each other and a turntable to rotate the inspected object. Those efforts developed transmission imaging with excellent contrast using a wide cone beam, induced-reaction imaging techniques that can reconstruct images of the probability of induced fission and hydrogen elastic scattering, and induced-reaction imaging techniques that can reconstruct images of the probability of inelastic neutron scattering (based on detected gamma rays) [1]–[3]. In addition, progress was made toward developing imaging techniques whose contrast originates from small angle scattering [4].

The goal of the present effort is to transition API techniques from laboratory to field use. In addition to limiting imaging to a single or few views, to permit field use, the source and detector panel must be portable, and the imaging process must work when the source and detector are positioned by hand rather than held in registration by a gantry. Hand positioning implies that each measurement has a unique source-detector placement, and this unique placement presents several challenges to API measurements. For instance, the usual practice of measuring a *void*, or normalization, measurement in the same configuration without the object present is not possible. In addition to providing the unimpeded counts in the detector, the normalization measurement typically determines which alpha and neutron pixels are in coincidence and their relative timing for subsequent analysis of imaging measurements. The size of the detector panel is such that radiographing most items, such as a 55-gallon drum, requires the detector panel to be moved to multiple positions within the coincident cone of tagged neutrons, and then those images must be stitched together to produce an image of the item. To form a useful composite image, the multiple images must be accurately stitched together despite the relatively low resolution of the detector panel and small number of overlapping pixels.

Addressing these challenges required the development of new techniques. This new paradigm first requires robustly characterizing the imaging system to determine timing alignment for all the neutron and alpha detector pixels, the efficiency map for the pixels of the neutron detector, and the direction vector and characteristic width for neutrons associated with each alpha detector pixel. Using these characterization data, the position and orientation of the neutron detector panel relative to the source can be inferred from coincidence data for each measurement. The distance from the source to each neutron detector pixel is inferred primarily from the neutron time of flight (TOF). Likewise, the detector position within the neutron coincidence cone (perpendicular to the direction of neutron travel) is determined primarily from the alpha pixels that are coincident with each neutron detector pixel. The inferred detector position, combined with source and panel characterizations, enable calculation of an expected void measurement. The inferred detector positions also enable projection of multiple images into a common plane to form a stitched image. Despite the relatively low detector panel spatial resolution, accurate stitching can be achieved without requiring overlapping neutron detector panel locations.

1.1 THE API SYSTEM

The API technique is illustrated schematically in Figure 1. A fast-timing position-sensitive alpha-particle detector inside the D-T neutron generator records the time and position of alpha-particle detections. Likewise, a position-sensitive fast-neutron detector records the time and position of neutrons. Nanosecond times and pixel numbers (locations) are recorded for each interaction above threshold, and coincidences are formed during analysis.

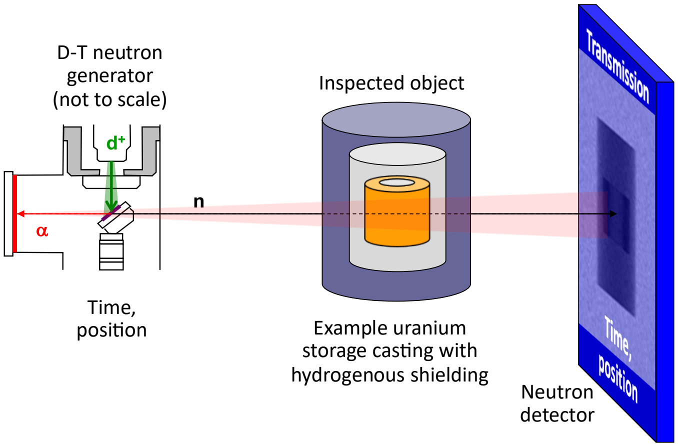

Figure 1. Schematic diagram of an exemplar system using the API technique.

Because the alpha particle and neutron are emitted simultaneously in (nearly) opposite directions, detection of the time and position of the alpha particle determines the time and direction of the associated neutron. In the coincidence data, transmitted, scattered, and induced neutrons are identified by their arrival times, positions, and number. Transmission imaging is performed when no interactions occur between the source and detector, and the transmitted neutron is detected on the other side of the object. The transmitted neutrons decrease with thickness of the object like $e^{-\mu x}$, where μ is the attenuation coefficient (the reciprocal of the mean free path) for 14.1 MeV neutrons, and x is the path traversed through the object. A transmission radiograph gives an image of μx along each path through the object from the source to the detector pixel, and the radiograph is extracted from measured data by taking the logarithm of the ratio of the number of neutrons with and without the object present.

The neutron source for the present API system consists of a Thermo Fisher API-120 DT neutron generator [5]. The alpha detector inside the neutron generator consists of a 50 mm diameter by 0.1 mm thick YAP:Ce scintillator coated on one side with 1.6 μm of aluminum that grounds the detector and blocks scattered beam and light from ionization within the neutron generator. Scintillator light from the alpha detector exits the neutron generator vacuum through a Schott 75C fiber-optic window that preserves its position information. Readout of the scintillation light from the alpha detector employs a Hamamatsu H13700 multi-anode photomultiplier tube (PMT), which is optically and electronically segmented into four quadrants. Each quadrant employs a four-corner resistive readout and a 256-pixel fused-silica optic, which discretizes and linearizes the response. Centroiding of the four corners is used to identify each pixel. Photographs of the alpha-particle detector at different stages of assembly, and mounted on the detector, are shown in Figure 2. Optical segmentation into readout quadrants is visually apparent in the light guides shown in Figure 2c. The quadrants are equal in area, but two of them are not square to avoid having four quadrants meet in the center of the field of view.

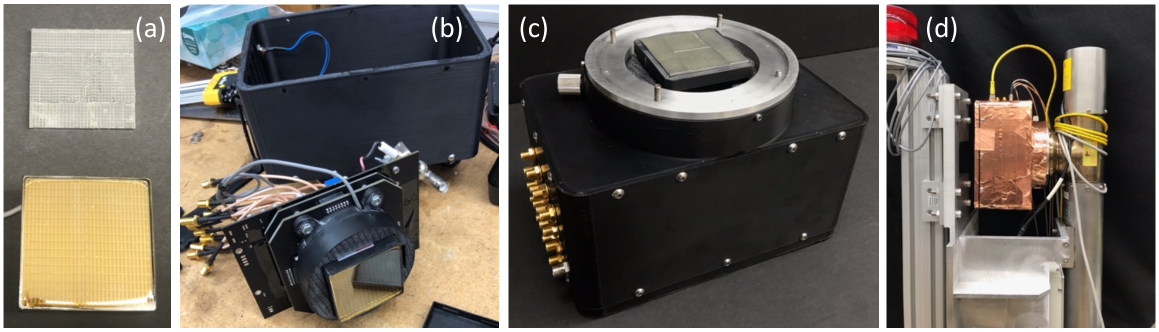

Figure 2. Photographs of the alpha-particle detector during different stages of assembly. (a) The PMT and light guides, (b) the PMT mounted on the resistive division boards, (c) the assembled detector, and (d) the assembled detector mounted on the D-T neutron generator.

Signals from the alpha-particle detector are recorded by a Struck SIS3316 waveform digitizer mounted to the D-T neutron generator stand, and data are read via a front-panel gigabit Ethernet connection using custom data acquisition software. The digitizers used for the alpha-particle and neutron detectors are synchronized using a custom clock card that distributes clock time to the front-panel low voltage differential signaling (LVDS) connectors on the SIS3316 modules. Photographs of the digitizer enclosure mounted to the neutron generator are shown in Figure 3. In the photograph on the right, the clock board, 10 Gb Ethernet switch, and SIS3316 digitizer are visible from left to right.

Figure 3. The data acquisition enclosure. (*left*) Enclosure mounted to the neutron generator stand and (*right*) a close-up showing the clock board, 10 Gb ethernet switch, and digitizer board.

The neutron detector panel consists of a 30 × 30 array of 10.4 × 10.4 × 50 mm pixels of EJ-299-33M scintillator capable of pulse-shape discrimination (PSD). The panel has been described in the literature [6]. However, for completeness, Figure 4 shows photographs of the detector during assembly that reveal the scintillator array.

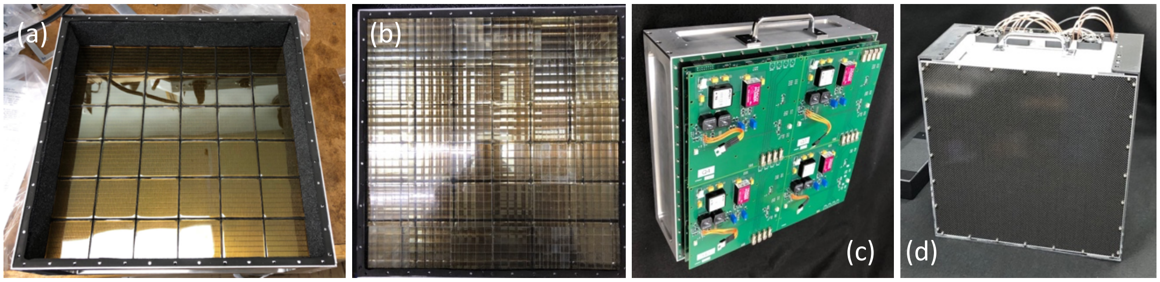

Figure 4. The neutron detector panel. (a) Panel before installation of the scintillator array, (b) after installation of scintillator array, (c) the completed scintillator module, and (d) the fully assembled detector panel.

Excluding the handle, the neutron detector panel has external dimensions 33.1 × 33.1 × 14 cm and weighs 18.6 kg, of which approximately 4.9 kg is scintillator.

2. DETECTOR CALIBRATIONS

2.1 CALIBRATION MEASUREMENTS

Before the relative positions of the API neutron generator and the neutron panel may be inferred from coincidence data, various calibrations must be established. Chief among these are (1) the neutron- and alpha-pixel-dependent time shifts and (2) the neutron direction centroids of the neutron cones defined by each alpha pixel.

To perform this characterization, the neutron panel was positioned with its front face 64.55 cm from the D-T spot. At this distance, the neutron panel does not cover the full field of view of neutrons coincident with the alpha-particle detector. Therefore, the panel was placed on a remotely controlled horizontal translation stage allowing for precise lateral ($\hat{x}$) movements, as seen in Figure 5. The D-T generator was located on a stand allowing for manual vertical ($\hat{y}$) movements. The combination of these relative vertical and horizontal motions allowed for coverage of the full coincidence cone of tagged neutrons by using a series of twelve measurement positions. At each position, 10 min measurements provided $O(1{,}000)$ coincident events per neutron pixel at each location.

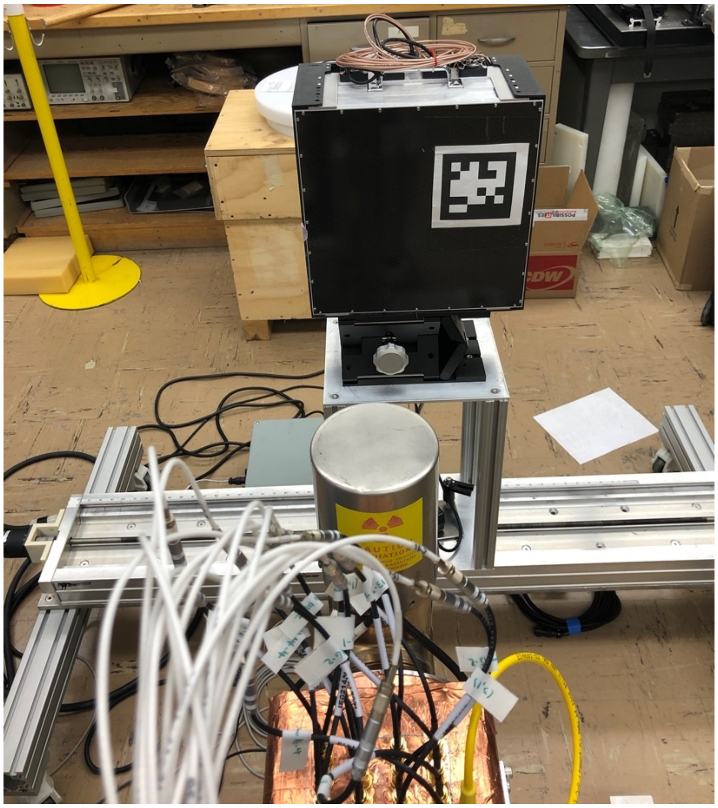

Figure 5. Detector setup for calibration measurements. The neutron panel was located on a horizontal stage allowing for left-right movements. The D-T generator (located at the bottom of the image) could be moved vertically allowing for the alpha coincidence cone to be measured top-bottom.

Data were recorded in a 3 × 4 grid of neutron detector positions with lateral spacing of 15.24 cm. The bottom three rows of measurements were also separated by 15.24 cm with the second row centered on the D-T spot of the neutron generator. This spacing (roughly half the neutron panel width) allowed sufficient overlap to prevent dead spots in the scanned *xy* plane and allowed for multiple measurements of the central alpha-pixel directions to cancel potential systematic effects originating from nonuniform responses across the face of the neutron panel. The fourth row of measurements was separated from the row below by 10.16 cm. This additional height was necessary to scan the full coincidence cone because the overall direction of the coincidence cone is tilted toward the neutron generator axis by about 4° by the momentum of the mixed D-T beam from the ion source. In the given orientation of the neutron source, the center of the coincidence cone is higher than the D-T neutron spot because of this expansion. Detector locations for the characterization measurements are summarized in Table 1.

Table 1. Calibration measurement geometries used to evaluate timing calibrations and alpha-pixel-defined neutron unit vectors

Position	*x*-coordinate (cm)	*y*-coordinate (cm)	*z*-coordinate (cm)
1	−15.24	15.24	64.55
2	0.0	15.24	64.55
3	15.24	15.24	64.55
4	−15.24	0.0	64.55
5	0.0	0.0	64.55
6	15.24	0.0	64.55
7	−15.24	−15.24	64.55
8	0.0	−15.24	64.55
9	15.24	−15.24	64.55
10	−15.24	−25.4	64.55
11	0.0	−25.4	64.55
12	15.24	−25.4	64.55

Note: The *z*-coordinate is measured from the neutron panel front face to the D-T spot.

For the subsequent discussion, the following right-handed coordinate system was used (looking from the D-T generator to the neutron panel):

- $+\hat{x}$: directed to the right
- $+\hat{y}$: directed down
- $+\hat{z}$: along the beam axis
- The origin $(0,0,0)$ is defined as the location of the D-T spot.

The coordinate system is illustrated by the schematic diagram in Figure 6.

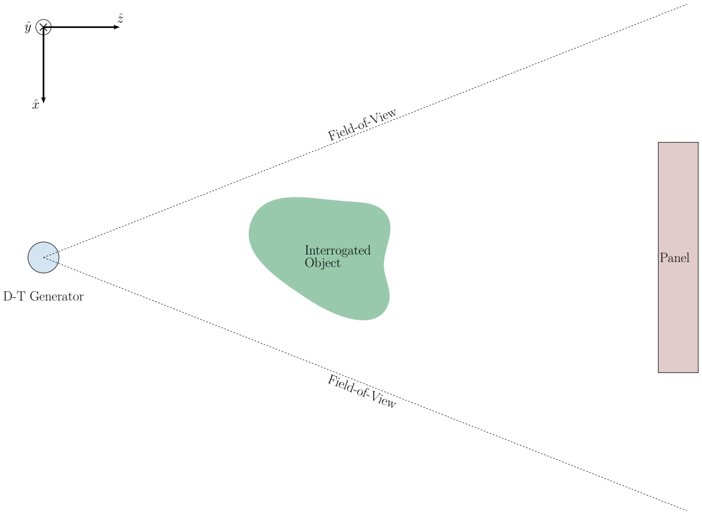

Figure 6. Top-down view of a measurement schematic showing the coordinate system used to measure alpha-cone directions and evaluate the source-detector geometry. Positive $\hat{x}$ is directed toward the bottom of the figure, positive $\hat{y}$ is directed into the page, and positive $\hat{z}$ is directed along the beam axis. The D-T spot is defined as the origin.

2.2 TIMING CALIBRATIONS

The relative timing between an alpha particle and a coincident neutron is affected by a combination of factors that includes various electronics delays and the neutron TOF:

$$t_{\mathrm{n}} - t_{\alpha} \equiv t_{\mathrm{TOF}} + t_{n}^{\mathrm{Elec.}} + t_{\alpha}^{\mathrm{Elec.}}, \tag{1}$$

where t_{n} and t_{α} are the measured times of the neutron and alpha-particle interactions under consideration, respectively, t_{TOF} is the expected TOF for a 14.1 MeV neutron detected in the neutron pixel, and $t_{\mathrm{n}}^{\mathrm{Elec.}}$ and $t_{\alpha}^{\mathrm{Elec.}}$are the electronic delays associated with signals from the neutron and alpha-particle pixels under consideration, respectively. In addition to the more typical electronic delays (e.g., PMT transit times, signal propagation times through cables), the resistive networks on both the neutron panel and the alpha-particle detector, which provide the segmented readouts, introduce pixel-dependent timing delays that must be accounted for. An alpha-particle TOF that depends on alpha pixel is also present, but in this analysis, it is subsumed into the electronic term.

When the location of the neutron panel is known, the expected neutron TOF contribution to the relative neutron/alpha-particle timing may be subtracted, isolating the electronics contributions to the relative timing:

$$t_{\mathrm{n}} - t_{\alpha} - t_{\mathrm{TOF}} = t_{\mathrm{n}}^{\mathrm{Elec.}} + t_{\alpha}^{\mathrm{Elec.}}, \tag{2}$$

In the absence of any electronics delays, this calculation should produce a distribution centered on the origin (with a width given by the timing resolution of the neutron panel–alpha-particle detector system). Any deviation from zero can be directly attributed to the various electronics delays in the system. The neutron- and alpha-pixel-dependent delays cannot be directly separated from each other (although the use of multiple source-detector geometries minimizes this degeneracy by placing different neutron pixels in coincidence with different alpha-particle pixels). Therefore, an iterative approach to evaluating the timing calibrations was adopted:

1. Form neutron TOF-subtracted time difference vs. alpha-particle pixel distributions (applying current neutron/alpha-particle pixel timing calibrations).

2. For each alpha-particle pixel time difference spectrum, fit the neutron transmission peak with a Gaussian with an exponential tail [7].

3. Update the alpha-particle pixel timing calibration with the mean of the best-fit Gaussian.

4. Form neutron TOF-subtracted time difference vs. neutron pixel distributions (applying current neutron/alpha-particle pixel timing calibrations).

5. For each neutron pixel time difference spectrum, fit a Gaussian with an exponential tail to the neutron transmission peak.

6. Update the neutron pixel timing calibration with the mean of the best-fit Gaussian.

7. Form gamma TOF-subtracted time difference vs. alpha-particle pixel distributions (applying current neutron/alpha-particle pixel timing calibrations).

8. For each alpha-particle pixel time difference spectrum, fit a Gaussian with an exponential tail to the gamma transmission peak.

9. OPTIONAL: Update the alpha-particle pixel timing calibration with the mean of the Gaussian.

10. Proceed to Step 1.

For ease of reference, the functional form of the Gaussian with an exponential tail is included:

$$f(t) = r + A\begin{cases} \mathrm{e}^{-0.5\left(\frac{t-\mu}{\sigma}\right)^2} \text{ for } \dfrac{t-\mu}{\sigma} < k \\ \mathrm{e}^{\frac{k^2}{2}-\frac{k(t-\mu)}{\sigma}} \text{ otherwise} \end{cases}, \tag{3}$$

where μ represents the Gaussian mean, σ is the Gaussian width, k demarcates the transition from the Gaussian to exponential shape, and r represents the randoms rate.

For some alpha-particle pixel time difference spectra, the statistics of the gamma peak are not adequate for a successful fit. In this case, only the neutron transmission peak is used to update the alpha-particle pixel timing calibration. The change in the measured TOF spectra throughout a single timing-calibration iteration is shown in Figure 7. The oscillations at the neutron transmission peak as a function of pixel number are caused by the resistive readout: with the start/end of an oscillation corresponds to the transition from one pixel row to the next.

The gamma TOF is incorporated into the calibration scheme to eliminate a random walk in the relative alpha-particle pixel times from one side of the alpha-particle detector to the other. This walk can accumulate in the calibration process using neutrons alone in proportion to the square root of the number of steps across the detector required to tie the timing of the alpha-particle pixels on one side of the detector to the alpha-particle pixels on the other side of the detector. Unfortunately, when using the gamma times, a slight systematic shift in the neutron TOF-subtracted timing spectrum that persists across all iterations followed the gamma correction (Figure 7d). The gamma TOF subtraction currently assumes the gamma rays are produced at the D-T target and that they interact on average at the same pixel depth as the 14.1 MeV neutrons. Neither of these assumptions are likely true, and further study is needed to evaluate the average production and interaction locations of these inelastic gamma rays. The current version of the gamma-flash-based timing calibration update introduces a systematic shift of roughly 160 ps in the neutron TOF spectrum (corresponding to roughly 0.8 cm for a 14.1 MeV neutron). This shift introduces a bias into the panel position fit. For this reason, the gamma-flash update is not used at this time.

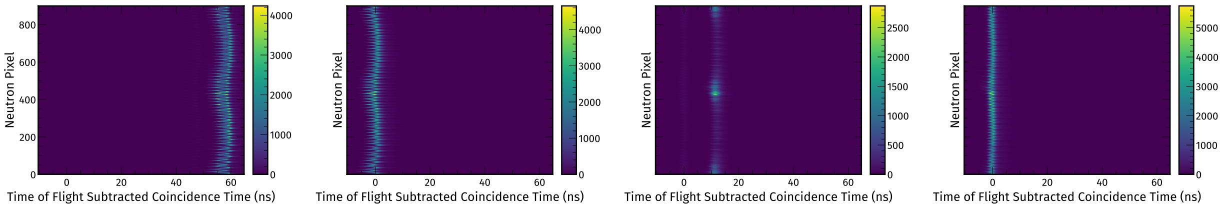

(a)

(b)

(c)

(d)

Figure 7. Change in the measured TOF-subtracted time neutron-alpha time difference throughout a single iteration of the neutron/alpha-particle pixel timing calibrations. (a) The original neutron TOF-subtracted spectra vs. neutron pixel number before any timing calibrations, (b) the spectra after the alpha-particle pixel calibrations update, (c) the spectrum after the neutron pixel calibrations update, and (d) the spectrum after the gamma peak correction. Note that figure (c) includes a subtraction of the gamma TOF (rather than a neutron TOF) and includes a pulse shape cut to help identify the gamma peak (the faint band centered at *t* = 0 ns).

The number of timing calibration iterations for the finalized timing calibrations must be selected. To make this selection, the timing spectrum after each round of iterations was integrated over all alpha-particle and neutron pixels. This spectrum was then fit with the same Gaussian with an exponential tail shape used to fit the pixel-dependent time spectra during the iteration. The Gaussian full width at half maximum (FWHM) of the 14.1 MeV neutron transmission peak from these fits was examined as a function of iteration number, as shown in Figure 8. After roughly five iterations, the timing resolution of the alpha-particle detector–neutron panel system exhibits diminishing returns on improvement: the resolution is 1.7 ns FWHM. For this reason, the pixel-dependent timing calibrations after five iterations were used in subsequent analyses.

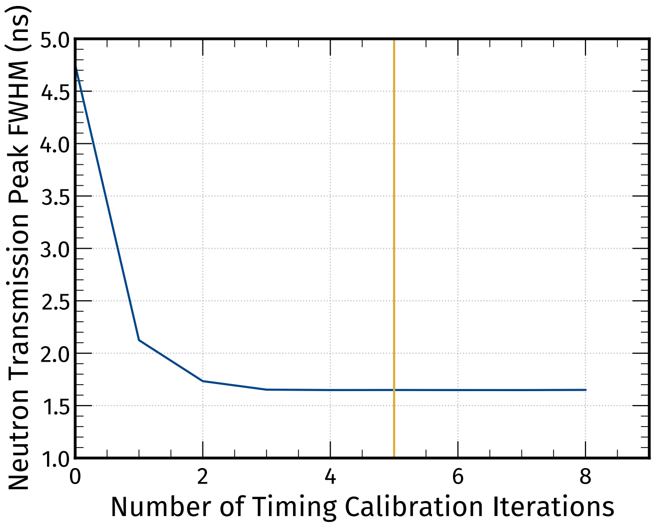

Figure 8. Timing resolution of the 14.1 MeV neutron transmission peak as a function of the number of pixel timing calibration iterations. The vertical orange line demarcates the number of iterations used in subsequent analyses.

Figure 9 shows the neutron TOF spectrum for raw (uncalibrated) time spectrum and the time spectrum after five iterations over the pixel timing calibrations. Implementing neutron and alpha-particle pixel-dependent timing calibrations improves the timing resolution by roughly a factor of 3 from a FWHM of 4.7 to 1.7 ns for the combined alpha-particle/neutron detector system.

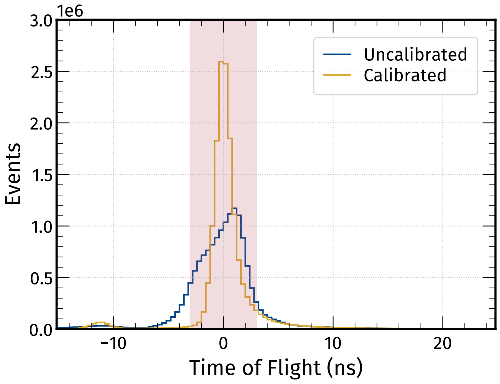

Figure 9. Neutron TOF-subtracted coincidence time spectra integrated over all neutron and alpha-particle pixels. Shown are the raw (uncalibrated) time spectrum in blue and the time spectrum obtained from the iterative calibration procedure after five iterations (orange). The uncalibrated spectrum (equivalent to the projection of Figure 7a to the time axis) was shifted to have a mean of $t = 0$ ns to facilitate visual comparison. The shaded box represents the TOF cut used when measuring the alpha-particle pixel directions.

2.3 DIRECTION CALIBRATIONS

The time-calibrated data measured the centroid of the neutron direction distribution defined by each alpha-particle pixel. To identify the neutron centroid and minimize systematic pulls on the evaluated centroid owing to scattered neutrons, a TOF cut isolated transmitted 14.1 MeV neutrons. A TOF cut of $-3 < \Delta t < 3$ ns in the TOF-subtracted coincidence spectrum was used, as illustrated in Figure 9.

The neutron hit pattern for each alpha-particle pixel coincident with the neutron panel was then fit with a 2D Gaussian, as shown in Figure 10. Only neutron pixels with an event count greater than 10% of the maximum event rate coincident with a given alpha-particle pixel were included in the fit. The centroid of this Gaussian fit, in conjunction with knowledge of the relative positions of the D-T generator and the neutron panel, was then used to evaluate the direction of the alpha-particle pixel-defined neutron cone.

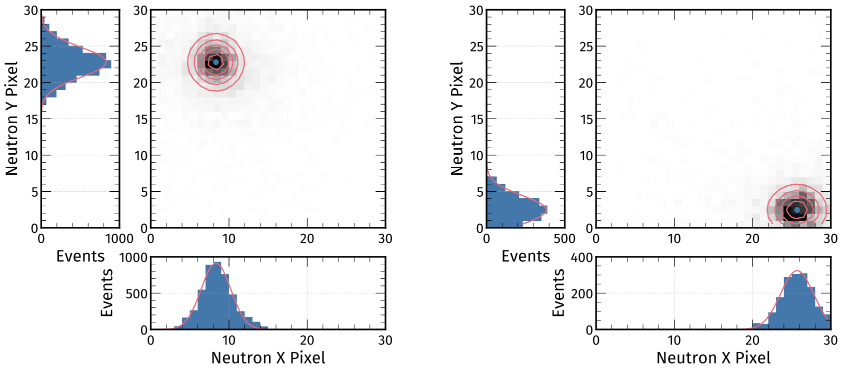

Figure 10. Example alpha-particle pixel neutron hit patterns. Overlaid are the centroid (marked with the teal dot) and contours from a 2D Gaussian fit to the hit pattern for pixels with an event count greater than 10% of the maximum. This 10% cut has been implemented on the *x* and *y* projection plots.

The results from all the fits to the alpha-particle directions are shown in Figure 11. The left panel shows that some alpha pixels were coincident with the neutron panel for multiple calibration datasets. For these pixels, the direction of alpha-particle pixel *i* ($\vec{\alpha}_i$) was implemented as the weighted average of the evaluated alpha-particle directions ($\vec{\alpha}_{ij}$):

$$\vec{\alpha}_i \equiv \frac{\sum_j \vec{\alpha}_{ij} w_{ij}}{\sum_j w_{ij}}, \quad w_{ij} \equiv \vec{\alpha}_{ij} \cdot \vec{d}_j^{\text{panel}}, \tag{4}$$

where $\vec{d}_j^{\text{panel}}$ is the unit vector pointing to the panel center for position *j*. At present, the weights provide a weak preference for alpha-particle directions measured near the center of the detector proportional to the cosine of the angle between the given vector and the center of the panel, but future weighting schemes are expected to more strongly penalize directions measured near the detector's edges. Alpha-particle directions are not included in the averaging if the Gaussian means in either the *x*- or *y*-pixel were within two pixels of the detector edge. This strategy prevents systematic biases caused by inadequate detector coverage of the full alpha-particle pixel-defined cone, as evidenced by the systematic pulls seen in Section 2.3.1.

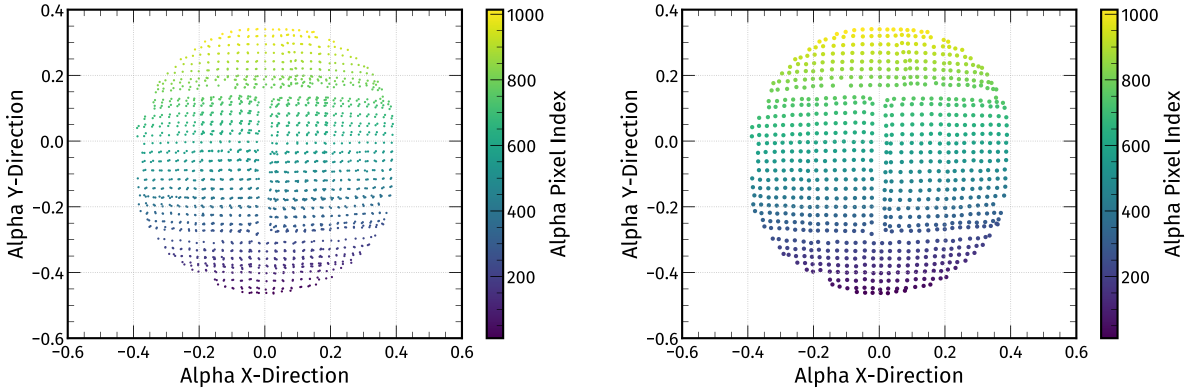

Figure 11. Alpha-particle pixel-defined unit vector *x* and *y* components. (*left*) Results from individual alpha-particle cone fits from each of the 12 calibration datasets. (*right*) Final alpha-particle unit vectors after individual fits were averaged.

The final evaluated alpha-particle directions are also shown in the right panel of Figure 11. The gaps visible in the alpha-particle direction map correspond to the boundaries of the four light guides/resistive readout networks on the alpha-particle detector.

2.3.1 Simulations to Investigate Systematic Effects

A series of radiation transport simulations were performed to investigate potential systematic errors associated with inferring alpha-particle pixel directions from alpha-particle/neutron coincidence data. In particular, simulations were run to evaluate potential systematic errors caused by the changing incidence angle as the coincidence cone is scanned and to evaluate potential systematic errors across the face of the neutron panel owing to the resistive readout network. These simulations indicated no significant systematic effects as a function of the neutron's incidence angle or across the panel face, and they demonstrated the importance of using all the available information (i.e., averaging results across multiple source-detector geometries when applicable) when evaluating the alpha-particle pixel-defined neutron directions.

The detector simulations were run using the `g4simple` [8] simulation package; `g4simple` is a Geant4-based [9]–[11] simulation framework that uses geometry definition markup language–defined geometries and the Geant4-provided physics lists, allowing for quick prototyping and simulation studies. These simulations were run with Geant4 10.5.p01 using the physics list QGSP_BERT_HP, which uses the Geant4 high-precision neutron physics lists under 20 MeV.

Figure 12 shows the simulated geometry of the neutron panel used to investigate various systematic effects on the evaluation of the alpha-particle pixel directions. The simulation included realistic materials and dimensions of the detector housing and scintillator blocks. No volumes representative of the PMTs are included at this time. The 14.1 MeV neutrons were simulated from a point source, and no volumes representative of the D-T generator were included. Consequently, effects from scattering in the neutron generator are not included in these simulations.

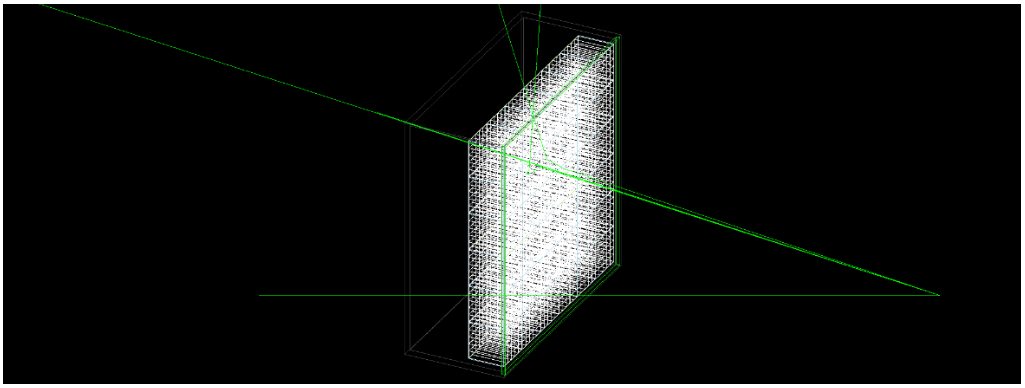

Figure 12. The 3D event display of the neutron panel Geant4 simulation geometry with four simulated 14.1 MeV neutron events. The simulation includes realistic representation of the scintillator blocks and detector housing. Currently no representative PMT or D-T generator volumes are included.

The output of the `g4simple` simulation is an event list that includes stepwise information about scatters in user-defined volumes (in this case the scintillator volumes). The pixel of interaction was initially calculated using a simple weighted average calculation. Ultimately, an Anger logic readout was implemented to reflect the actual panel readout more closely.

The weighted average calculation simply calculated the average *x*- and *y*-pixel locations of the energy depositions in the scintillator (weighted by the energy deposition at each step), accounting for effects of the quenching of nuclear recoils. This average location was then attributed to a given scintillator pixel, producing the hit pattern shown in the left panel of Figure 13 for a uniform source of 14.1 MeV neutrons.

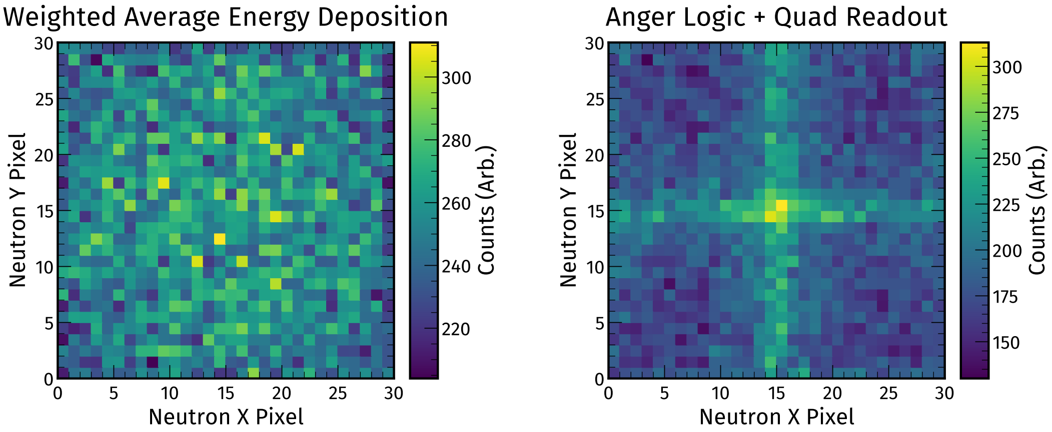

Figure 13. Pixel hit map from the Geant4 simulation. (*left*) Using a simple weighted average energy deposition and (*right*) using a simulated Anger logic readout. Note the simulated Anger logic readout shows the same cross pattern that is seen in data from intra-detector scattering.

The Anger logic implemented on the neutron panel was simulated via the following method:

1. The 30 × 30 pixel grid was divided into four 15 × 15 quadrants to mimic the physical panel readout.
2. The average pixel in each quadrant with an energy deposition was calculated by using the measured floods.
    - A 2D Gaussian fit to each pixel in the measured floods was sampled to calculate the average location in flood space.
3. The measured pixel look-up tables were used to attribute the average energy deposit location in flood space to a single scintillator pixel.

Simulated events with detector scatters across multiple quadrants result in events being detected in each quadrant for which a registered scatter occurs. These inter-quadrant scatter events typically occur near the borders of the readout quadrants, producing the cross shape seen in the right panel of Figure 13, which is also observed in the measured data. However, these effects may be minimized with suitable timing and pixel cuts.

A uniform cone of 14.1 MeV neutrons with an opening angle of 69° was simulated. This cone was then reweighted to represent the grid of neutron cones that would be defined by a 32 × 32 grid of alpha-particle pixels. The individual alpha-particle pixel-defined cones were assumed to have a 2D Gaussian shape with a FWHM of 4.5° and centers spaced by 1.5°. To cover the full cone, a 3 × 3 grid of source-detector geometries was simulated. The grid included $z = 53.12$ cm, $x = \pm 15.0$ cm, and $y = \pm 15.0$ cm, where the *z*-coordinate represents the distance from the neutron source to the front of the simulated neutron panel front face along the *z*-axis. The *z* distance for these simulations was chosen to match an earlier calibration dataset from before the installation of the timing board.

The hit pattern defined by each of these alpha-particle pixels was then fit with a 2D Gaussian, analogously to the calibration data. Again, as in the calibration data, the centroid of this Gaussian can be converted to a neutron direction by employing knowledge of the simulated geometry. For cases in which a simulated alpha-particle pixel is detected in multiple source–neutron detector geometries, the calculated directions were averaged.

The accuracy of this process was evaluated for two cases:

1. Perfect source-detector geometry assumed
2. 2 mm uncertainty in the source–detector geometry.

To make potential systematic shifts more noticeable, the 2 mm uncertainty is a factor of 2 larger than the assumed positional uncertainty in the calibration datasets. This uncertainty was implemented by randomly adding an offset to the true simulated geometry by sampling from a Gaussian distribution (with a mean of 0 mm and a standard deviation of 2 mm) in each of the x, y, and z directions. For the studies including position uncertainty, the offset was common to each pixel in each simulated source–panel geometry. However, no overall correlations existed between multiple source–panel geometries (i.e., no overall offset propagated to each simulation).

Figure 14 shows the results comparing the true neutron directions with the calculated neutron directions using the simulated neutron hit patterns. The top row represents the case in which the source–detector geometry is known perfectly. The bottom row represents the case in which a 2 mm uncertainty in the source-detector geometry was implemented for each simulated position. Averaging the measured direction across multiple source–detector placements helps remove the uncertainties in the source–detector geometry, as evidenced by the reduced tail at large angular mismatches for pixels for which multiple measurements of the alpha-particle direction may be evaluated.

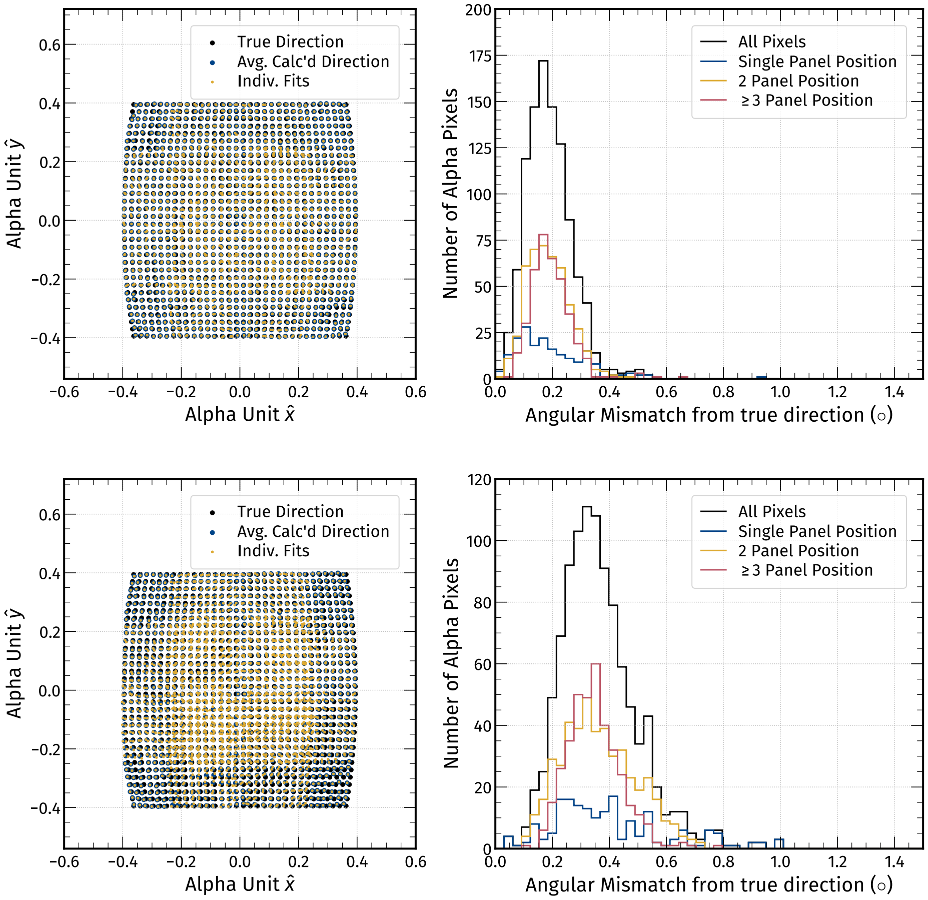

Figure 14, Comparison of calculated and true neutron-cone directions from simulated data. The top row shows the case of perfect panel positioning, whereas the bottom row has a randomly added 2mm position uncertainty applied to each simulated panel position. The left column shows the *x* and *y* unit vectors, and the right column shows the angular mismatch from the true neutron direction.

A similar investigation was performed using real data to examine the sensitivity to the assumed source–panel geometry by trying to replicate a single geometry by placing the panel by hand. Figure 15 shows the measured alpha-particle cone directions following multiple placements of the panel, including a case in which the panel was placed in nominally the same location, but rotated by 15° to look for any systematic effects caused by changing the incidence angle of the neutrons. No effect is seen beyond a global shift in the measured directions consistent with slight offsets in the source–detector geometry when placing the panel by hand, demonstrating the sensitivity to millimeter-scale differences in the panel placement.

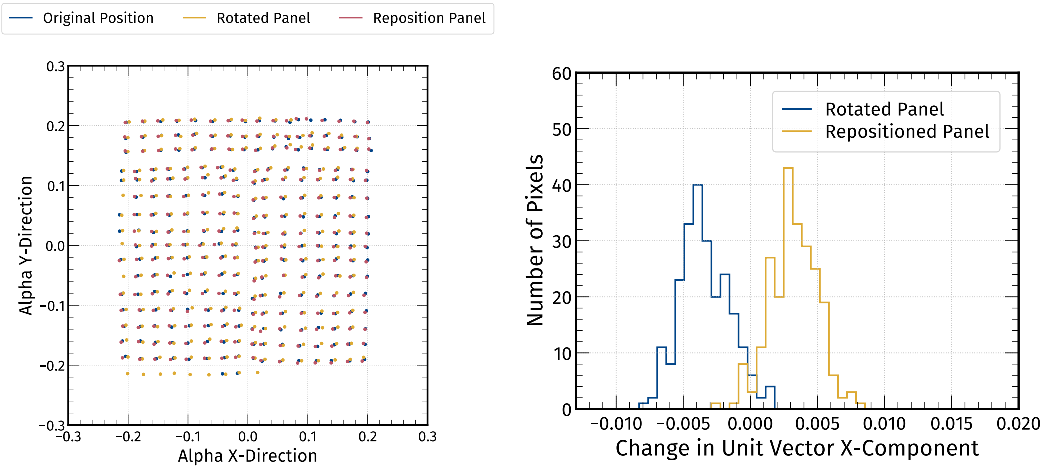

Figure 15. Sensitivity to panel placement. Millimeter-scale shifts in the panel placement following panel repositioning by hand are indicated by systematic shifts in the reconstructed alpha-particle directions. (*left*) The 2D distribution of the calculated x and y components of the alpha-particle pixel-defined unit vectors. (*right*) Change in the calculated alpha-pixel-defined unit vectors x component following repositioning of the panel.

Figure 16 shows the difference in the *x*- and *y*-components of the fit alpha-particle pixel direction compared with the true alpha-particle direction as a function of the mean pixel row or column of the 2D Gaussian fit for these simulated datasets. No noticeable systematic pulls are evident on the evaluated directions away from the detector edges. However, evidence of a systematic pull exists on the evaluated directions for alpha-particle cones near the panel edge of the panel owing to inadequate coverage of the alpha-particle pixel cone, introducing a bias toward the detected fraction of the cone. Because of this pull, pixels with a Gaussian mean (x or y pixel) within two pixels of the detector edge are not included the calculation of the alpha-particle cone directions as stated in Section 2.3.

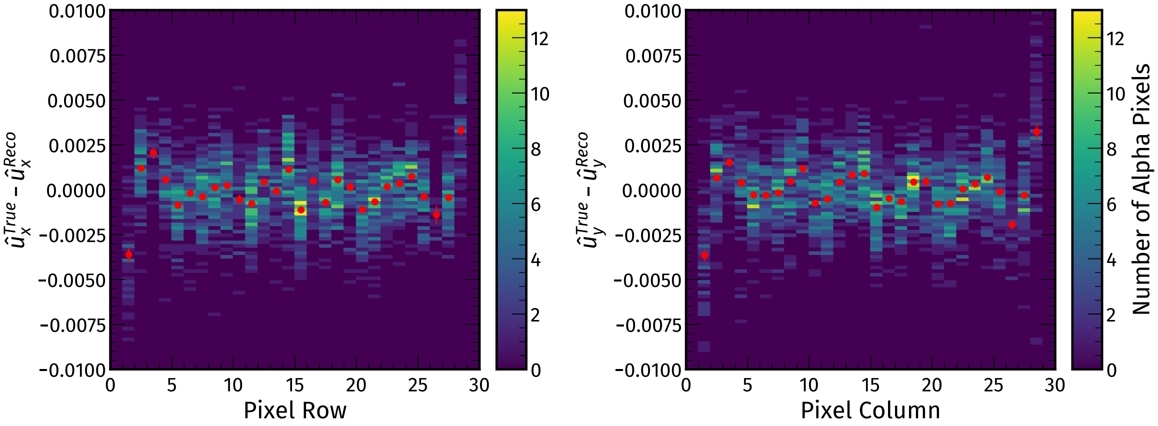

Figure 16. Difference in *x*- and *y*-components of the true and fit alpha-particle unit vectors as a function of the mean pixel row and column of the 2D Gaussian fit. The overlaid red datapoints represent the average value of each pixel row/column. No noticeable pulls are evident when the Gaussian means are more than two pixels from the detector edge.

Another set of simulations was run to verify the lack of any systematic pulls as the neutron's incidence angle is changed. For these simulations, a neutron cone defined by a single pixel (FWHM of 4.5°) was simulated. The panel was placed so that the neutron beam was directed at three locations on the panel:

1. Panel center
2. Center of a panel quadrant
3. Centered along the boundary between two quadrants

For each of these locations, the panel was rotated about its vertical axis in 5° increments up to an incidence angle of 45°. Angles above 45° are not anticipated during typical data collection from transmission-based measurements.

Again, the measured neutron direction was calculated by a 2D Gaussian fit to the neutron hit pattern for each source-panel geometry. Figure 17 shows the difference in the $\hat{x}$, $\hat{y}$, and $\hat{z}$ unit vectors between the measured and true neutron direction as a function of the mean incidence angle. No obvious systematic pulls are evident in the measured neutron direction as the neutron incidence angle increases, indicating that the changing incidence angle does not necessitate any corrections to the evaluated alpha-particle directions in the calibration data.

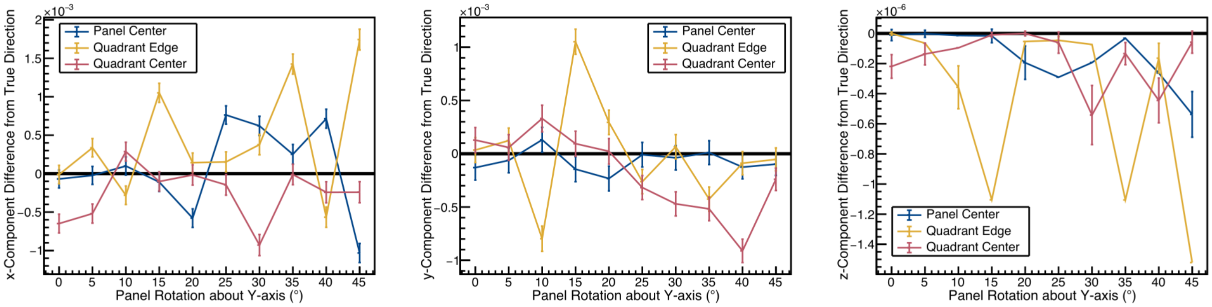

Figure 17. Difference between calculated and true neutron cone directions as a function of neutron incidence angle. No noticeable systematic pulls as a function of the incident angle are seen. Error bars arise from the statistical error on the Gaussian mean in the 2D Gaussian fits to the neutron hit pattern.

3. DETECTOR LOCALIZATION

This section details how the detector location is inferred from the alpha-particle/neutron coincidence data. Briefly, the position of each neutron pixel is determined from coincidence data: the direction to each neutron pixel is formed as a weighted average of the unit vectors of its coincident alpha-particle pixels, and the distance to each neutron pixel is determined from the TOF. Then, the best-fit position of the panel minimizes the sum-squared distance to the measured positions. This fitting process is sensitive to sub-millimeter position changes as inferred from the repeatability of sequential measurements without detector movement.

3.1 POSITION INFERRENCE VIA COINCIDENCE DATA

For any given neutron pixel in a transmission dataset, the alpha-particle cones coincident with that pixel and the timing of the neutron TOF peak are determined by the relative geometry between the D-T generator and neutron-detector panel. Therefore, the observed coincidences and peak times may be used to find the location of the panel relative to the generator without prior knowledge of the experimental setup. Although the directional error for an individual neutron pixel may be large owing to counting statistics, the combined error from 900 pixels will be quite small (barring systematic effects). The accuracy of this process inherently depends on the veracity of the ground-truth alpha-particle cone directions and timing calibrations described in the preceding section.

Unit vectors between the generator and each neutron panel pixel are established by taking the event-weighted average direction of all alpha-particle cones coincident with said pixel:

$$\vec{r}_n = \frac{\sum_i \vec{\alpha}_i w_i^n}{\sum_i w_i^n}, \tag{5}$$

where $\vec{r}_n$ is the unit vector for neutron pixel n, $\vec{\alpha}_i$ are the alpha-particle cone unit vectors from calibration, and w_i^n are the weighted number of coincident events between neutron pixel *n* and alpha cone *i*. The weights for coincident events are derived from the observed difference in emission rates for specific alpha-particle pixels. Neutron TOF peaks are fit using a Gaussian with an exponential tail (Eq. (3)), the same function used in deriving the time calibrations. An example fit is shown in Figure 19. The centroid μ of the Gaussian component of the fit is reported as the nominal TOF T_n^{Obs} between the generator and neutron pixel *n*.

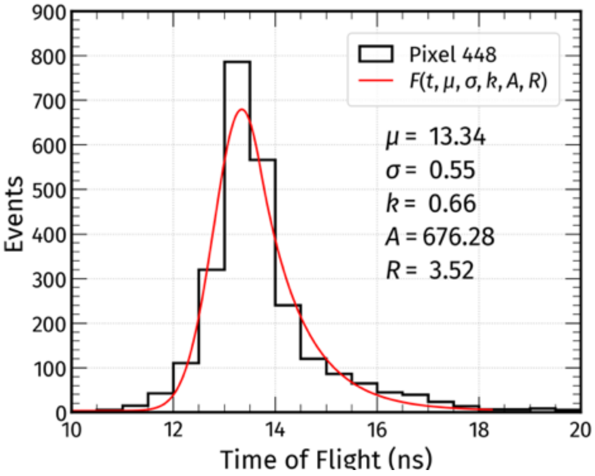

Figure 18. TOF spectrum for neutron events in pixel 448. Fit to data in red.

The resultant arrays of unit vectors and peak times serve as the input for the panel localization function. Selection criteria applied to the data before the TOF and unit vector calculations include

- A minimum alpha energy cut to eliminate accidental coincidences with x-rays
- Panel event energy between 350 and 2,460 keV selects unsaturated pulses large enough for adequate PSD
- PSD selection (0.8 < PSD parameter < 1.0) to select neutrons

An additional cut about the fit TOF for each neutron pixel ($-3 < T_n^{\text{Obs}} < 1.5$ ns) is also applied to ensure that direct-transmission neutron events are used for the panel localization. A 2D histogram showing alpha-particle pixels coincident with a single neutron pixel is shown in Figure 19a. This plot also shows several random coincident events in alpha-particle pixels that are unlikely to be on target with this specific neutron pixel. For neutron pixels that lie roughly in the center of the alpha-particle pixel phase space, the pull of these random coincidences will cancel each other out on average. However, neutron pixels on the edges of the alpha-particle cone will experience a systematic pull toward the center because no offsetting randoms occur beyond the edge of the cone. This pull produces a noticeable systematic bias toward the origin for neutron pixel unit vectors when the panel is positioned off-axis. This pull is addressed by limiting the number of alpha-particle pixels that contribute to the calculation of $\vec{r}_n^{\,p}$ to those that feature the largest number of coincidences. Presently, this strategy is implemented by only including alpha-particle pixels that have more than H_{min} coincident hits and is given by

$$H_{\mathrm{min}} = \mathrm{Max}\left(\frac{H_{\mathrm{max}}}{15}, 5\right),$$

where $H_{\mathrm{max}}$is the maximum number of coincident hits between any alpha-particle cone and neutron pixel n. The map of coincident alpha-particle pixels after applying this cut is shown in Figure 19b. Localization bias can also be introduced by including neutron pixels with low statistics that are caused either by lying outside the alpha cone or by the presence of several attenuation lengths of intervening material. A final cut requires that any neutron pixel vector used in the localization routine must have more than three hits coincident with a single alpha-particle pixel.

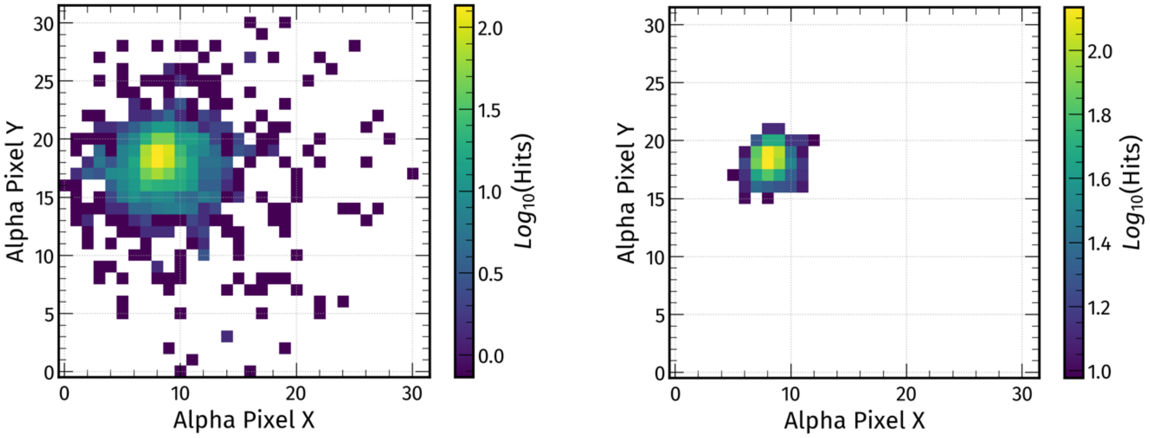

Figure 19. Map of coincident hits in alpha-particle pixel space for neutron pixel 448. (a) Before eliminating systematic bias toward the origin. (b) Map for the same neutron pixel after applying the minimum coincident hit cut.

Minimization of the panel localization function $F(\vec{P})$ returns a best fit six-component vector $\vec{P}(x, y, z, \theta_x, \theta_y, \theta_z)$ that specifies the translation and orientation of the detector panel with respect to the D-T generator. For a specific value of $\vec{P}$, the unit vectors ($\vec{r}_n^{\,P}$) and TOF T_n^P to each neutron pixel can be calculated. The function $F(\vec{P})$ takes the difference between these calculated vectors/TOFs and the arrays of directions and times ($\vec{r}_n$ and T_n^{Obs}) provided as input to the function:

$$F(\vec{P}) = \sqrt{\sum_n \left(\frac{|\vec{r}_n^{\,P} - \vec{r}_n|}{\langle \vec{r}_n \rangle}\right)^2 + \left(\frac{|T_n^{\mathrm{Obs}} - T_n^P|}{\langle T_n^{\mathrm{Obs}} \rangle}\right)^2}, \tag{6}$$

where $\langle \vec{r}_n \rangle$ and $\langle T_n^{\mathrm{Obs}} \rangle$ are the estimated error on the neutron pixel direction and peak time, respectively.

Minimizing the difference between the calculated and input values provides the best estimate of the true panel location.

3.2 LOCALIZATION PERFORMANCE AND SENSITIVITY

The panel localization method was applied to the void data used for geometry calibrations to assess its performance without the complication of attenuation from intervening material. The reconstructed and true positions for each of these runs are listed in Table 2. As expected, the localization routine performs well in the absence of any obstructing material. The set of geometry calibration runs yielded an average total positional error of approximately 2.4 mm. Most of the error in *xy* reconstruction is caused by residual pull toward the origin (as described in section 3.1). This error may be addressed in the future via appropriate random subtraction. Errors in *z* likely stem from multiple sources: assumptions in interaction depth, timing calibration errors, and geometry calibration measurement errors are potential culprits.

Table 2. Assumed true and reconstructed positions of the neutron panel using the localization routine

Position	***x* coordinate (cm)**		***y* coordinate (cm)**		***z* coordinate (cm)**	
	True	**Recon.**	**True**	**Recon.**	**True**	**Recon.**
1	−15.24	−15.26	15.24	14.86	64.55	64.42
2	0.0	−0.14	15.24	14.84	64.55	64.38
3	15.24	14.96	15.24	14.84	64.55	64.37
4	−15.24	−15.18	0.0	0.01	64.55	64.44
5	0.0	−0.06	0.0	−0.03	64.55	64.44
6	15.24	15.06	0.0	−0.04	64.55	64.40
7	−15.24	−15.12	−15.24	−15.26	64.55	64.60
8	0.0	0.03	−15.24	−15.34	64.55	64.51
9	15.24	15.14	−15.24	−15.27	64.55	64.51
10	−15.24	−15.05	−25.4	−25.41	64.55	64.79
11	0.0	0.04	−25.4	−25.45	64.55	64.72
12	15.24	15.26	−25.4	−25.39	64.55	64.76
Mean error	—	0.1	—	0.12	—	0.13

The inherent variability of the fit routine was examined by conducting a long duration run without changing the panel position and splitting the data into multiple sub-runs. Applying the localization routine to each subset then provides an estimate of the reproducibility of the position fit when using independent datasets. A measure of the inherent jitter also limits the expected minimum sensitivity to panel movement. Table 3 shows the observed standard deviation for the fit parameters when splitting a 900 s duration run into multiple runs that are independently fit.

Table 3. Standard deviation of fit parameters for subsets of long-dwell data

Sub-run duration (s)	**$\sigma(x)$ (cm)**	**$\sigma(y)$ (cm)**	**$\sigma(z)$ (cm)**	**$\sigma(\theta_x)$ (°)**	**$\sigma(\theta_y)$ (°)**	**$\sigma(\theta_z)$ (°)**
225	0.017	0.008	0.005	0.07	0.05	0.37
112.5	0.011	0.016	0.034	0.17	0.11	0.40
60	0.026	0.016	0.019	0.18	0.19	0.25

Fits to subsets of the long-dwell data demonstrate that the variability in the position fit is minimal (<0.5 mm) for void data. This behavior may not hold for measurements of highly attenuating objects for which the number of events per pixel is potentially orders of magnitude smaller. However, errors owing to systematic biases in alpha-particle/neutron pixel cuts are expected to dominate over the reduced statistics for position localization.

4. VOIDLESS NORMALIZATION

In gantryless API radiography systems, it will not always be possible to take a void measurement under the same conditions as the object measurement. Therefore, a method for calculating the number of mean free paths along a source–neutron pixel ray must be developed.

The measured number of alpha particles during the measurement of an object allows for calculating a voidless normalization by considering various detector effects. The process of calculating the voidless normalization can be summarized as follows, with details in the subsequent subsections:

1. Calculate a relative pixel-to-pixel efficiency correction for the neutron panel.

2. Measure the absolute detection efficiency for 14.1 MeV neutrons.

3. Project the alpha-particle pixel-defined cone onto the neutron panel, assuming a specific geometry, and fold it with the efficiencies above.

4. Sum the hit patterns for each coincident alpha-particle pixel.

4.1 RELATIVE PIXEL EFFICIENCY NORMALIZATION

The first step in calculating a voidless normalization is to evaluate the pixel-to-pixel differences of the neutron detection efficiency of the neutron panel. Although an energy acceptance window is defined to improve the uniformity of the detector response, pixel-to-pixel variations remain in the detection efficiency owing to, for example, light coupling efficiencies between the scintillator pixel and the various reflective surfaces.

Data were collected with the panel placed on an 80/20 stand and located on-axis at a distance of 81.1 cm (measured from the panel front face to the DT spot). The pixel efficiency was calculated for two cases:

1. Neutron panel singles data independent of an associated alpha tag
2. Requiring a neutron-alpha coincidence.

Requiring a coincidence with the alpha detector helps to remove contamination from e.g., room scatter.

The efficiency maps from these two methods are shown Figure 20. Figure 20a shows the efficiency map requiring an alpha tag, Figure 20b shows the efficiency map using neutron singles, Figure 20c shows the ratio of the two efficiency maps, and Figure 20d shows the average ratio value along each pixel axis. The efficiency maps are normalized to have an average value of 1. The statistical fluctuations on the number of events in each pixel are on the order of 1%.

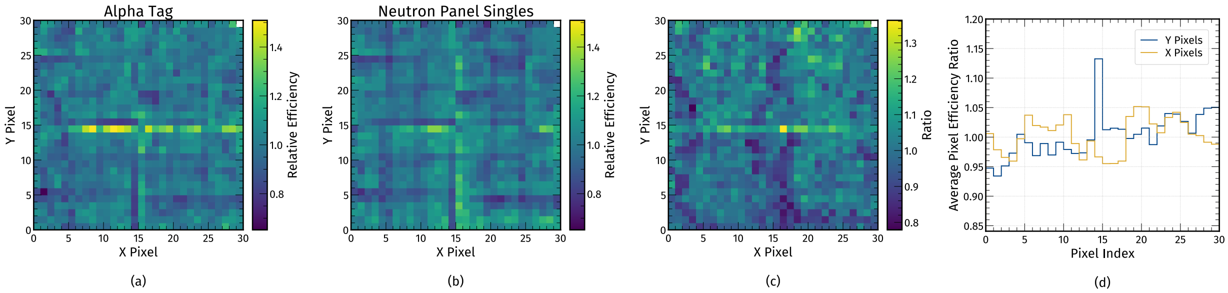

Figure 20. Relative neutron pixel efficiency correction to calculate the void-less normalization. (a): Pixel efficiency corrections for neutron panel hits with an alpha tag. (b) Pixel efficiency corrections for neutron singles (no alpha tag) data. (c) The ratio of the 2 efficiency maps showing a relatively higher apparent 14.1 MeV detection efficiency near the bottom of the neutron panel in the singles data due to contamination from e.g., room return. (d) Average ratio along each pixel axis.

Although the relative efficiencies for both cases are similar across the panel, some differences in the singles data, particularly along the bottom few rows of scintillator pixels, appear to indicate that the bottom of the panel is more efficient. This result is due to contamination from room-return events that artificially increase the calculated pixel efficiency. Room return from the laboratory floor and the 80/20 stand the detector was sitting on seem to have the most noticeable effect, as evidenced by the difference in the calculated efficiency, particularly for the bottom five rows of pixels. These effects are minimized when an alpha tag is required. Therefore, the efficiency map in which an alpha tag is required was used to construct the relative pixel efficiencies.

4.2 ABSOLUTE PANEL EFFICIENCY

The calibration datasets discussed in Section 2.1 were used to evaluate the absolute detection efficiency for 14.1 MeV neutrons. For each of these datasets, a tally of the detected number of neutrons for each alpha-particle pixel tag was created, allowing for a distribution of detection efficiency vs. alpha-particle pixel, as seen in the left panel of Figure 21. The efficiency values from each of the 12 calibration datasets were then histogrammed, as shown in the right panel of Figure 21. The peak of this distribution, representing alpha-particle pixels directed at the neutron panel, was fit with a Gaussian distribution, and the mean value of the Gaussian was taken as the absolute detection efficiency, yielding an efficiency of 3.3% within the energy acceptance window used (350 < E < 2,460 keVee). The detection efficiency could be increased by loosening this energy acceptance window at the cost of a less uniform detector response.

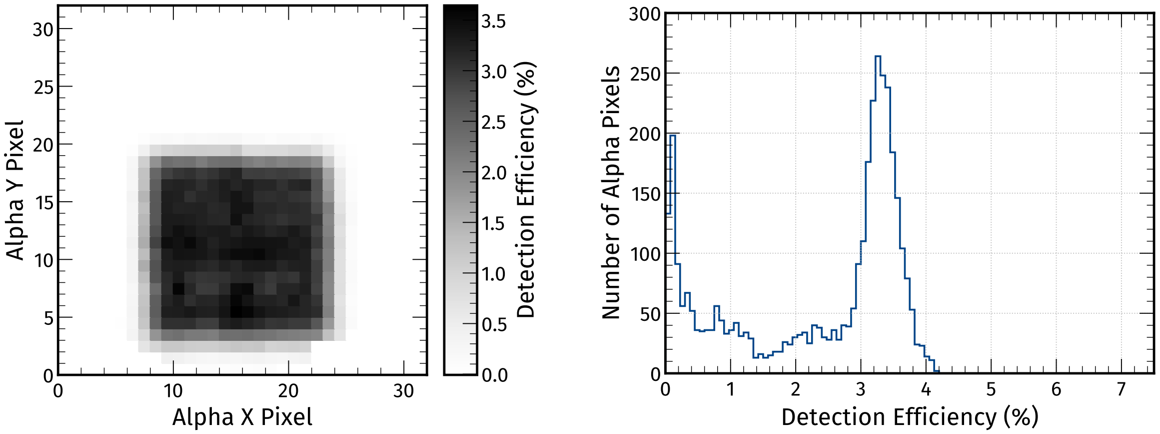

Figure 21. Absolute neutron panel detection efficiency. (*left*): Example efficiency vs. alpha pixel tag for a single calibration dataset. (*right*) Histogram of efficiency values for each of the 12 calibration datasets. The tail at lower efficiencies is due to alpha pixels directed away from the panel in which only part of the alpha-particle pixel-defined coincidence cone intersects the neutron panel.

4.3 ALPHA CONE PROJECTION

The source–detector geometry can be found from the data-driven algorithm in Section 3. In conjunction with the known alpha-particle pixel directions measured during the detector calibrations (Section 2.3), the alpha-particle pixel-defined cones may be projected onto the neutron panel. Although the width of each alpha-particle cone is different (and the widths in the *x* and *y* directions may also be different), currently the average cone width is assumed for each pixel (FWHM of 4°). The cones are assumed to have a 2D Gaussian shape.

By accounting for the total number of neutrons emitted in a given direction (as measured by the number of alpha particles detected in each alpha-particle pixel) and the neutron detection efficiency, the expected neutron panel hit pattern for each alpha-particle pixel tag with no intervening material may be calculated. These alpha-particle pixel-dependent hit patterns can then be summed to calculate the expected number of neutron coincidences on the panel for a given source–detector geometry.

The total number of neutrons detected by a given neutron pixel (r_i^n) is given by

$$r_i^n = A\epsilon_i\epsilon_{\mathrm{abs}}\sum_j^{N_\alpha} R_j^\alpha w_{ij}\Omega_i, \quad w_{ij} \equiv \frac{1}{2\pi\sigma_{j,x}\sigma_{j,y}}\mathrm{e}^{-\left(\frac{\theta_{ij,x}^2}{2\sigma_{j,x}^2}+\frac{\theta_{ij,x}^2}{2\sigma_{j,y}^2}\right)}, \tag{7}$$

where ϵ_i is the relative pixel efficiency for neutron pixel *i* (Section 4.1), ϵ_{abs} is the absolute neutron detection efficiency (Section 4.2), R_j^α is the measured rate in alpha-particle pixel *j*, and w_{ij} is the angular weighting factor dependent on $\theta_{ij,x/y}$ (the angle between the alpha-particle centroid and the neutron pixel) and $\sigma_{j,x/y}$ (the angular width in the x/y directions of the alpha-particle cone for pixel *j*, here assumed to be 4° FWHM). Pixels are only included in the sum for values of $w_{ij} > 0.1$. The fraction of the solid angle subtended by the cross section of a neutron pixel *i* is Ω_i. The correction factor A depends on the distance of the panel to account for the numerical integration of the alpha-particle cone for distances above roughly 26 cm (from panel front face to the D-T spot or a total distance – as returned by the detector localization calculation – of roughly 29 cm from the D-T spot to the pixel center depth at the middle of the panel), as shown in Figure 22. The pixel center is located 3 cm behind the panel front face. This correction factor is given as:

$$A(d) \equiv \begin{cases} 1, & d \leq 28.6\ \mathrm{cm} \\ 0.05\mathrm{e}^{-(d-29.18)/18.8} + 0.9, & d > 28.6\ \mathrm{cm} \end{cases}, \tag{8}$$

where *d* is the distance from the D-T spot to the pixel center at the middle of the panel.

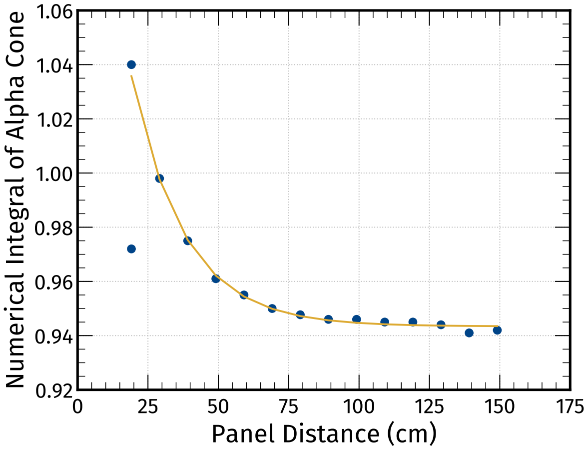

Figure 22. Numerical integration of alpha-particle cone across the face of the neutron panel as a function of distance for a cone pointed at the center of the detector. The distance is measured from the D-T spot to the panel front face. The orange curve is a fit to the data

Figure 23 shows an example of how the expected number of neutron coincidences is calculated. Shown are both the calculated and measured neutron hit patterns for a single alpha-particle pixel (top left and center), along with their ratio (top right), their projections to the *x* and *y* axes (bottom left), and the hit pattern summed over all alpha-particle pixel cones calculated at that point (bottom center and right). The entire alpha-particle cone is not included here because of the cutoff on w_{ij}, which creates a pixel mask that is also applied to the measured data.

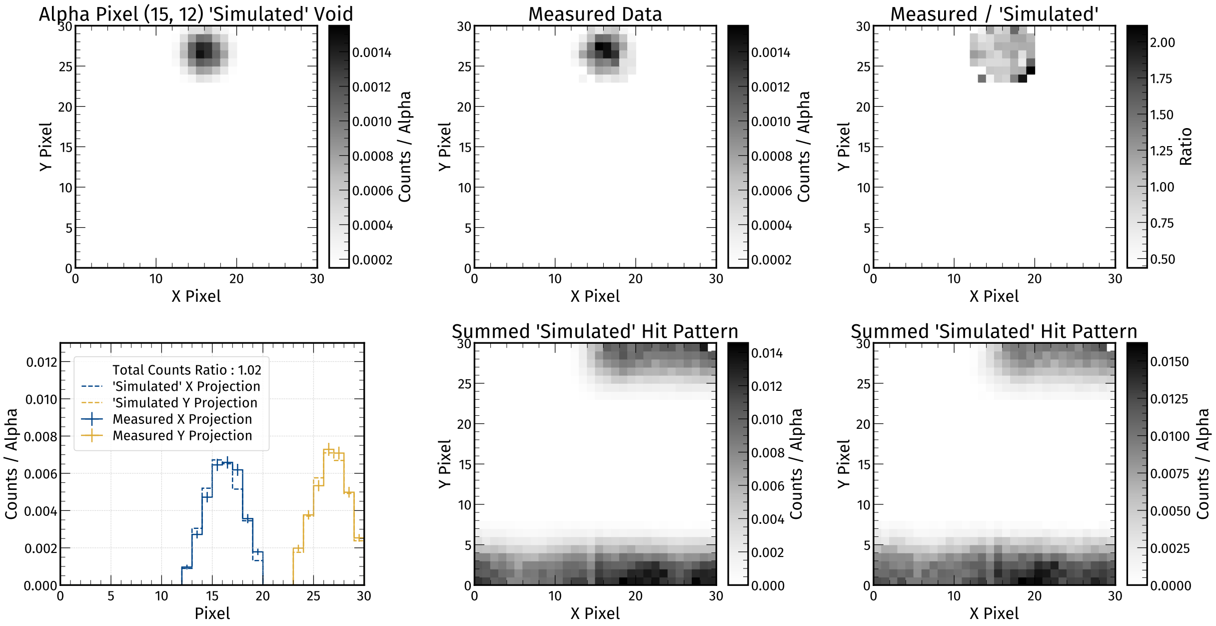

Figure 23. Voidless normalization. Shown in the upper left is the calculated, or simulated, void projection on the neutron panel for a single alpha-particle pixel. The upper center shows the measured hit pattern for that same alpha-particle pixel. The upper right is the ratio of the measured and simulated hit patterns. The lower left shows the hit pattern projections to the *x* and *y* axes for both simulated and measured data. The lower center shows the summed hit pattern over all alpha-particle pixels considered so far for the simulated void. The lower right shows the same distribution for the measured data.

4.4 APPLICATION TO DATA

4.4.1 Void Dataset

Figure 24 compares a calculated void with a measured void taken from the central position of the calibration dataset discussed in Section 2.1. By calculating the expected number of counts and comparing that with a void measurement (which this normalization is intended to replicate), the systematic uncertainties in the normalization calculation can be estimated.

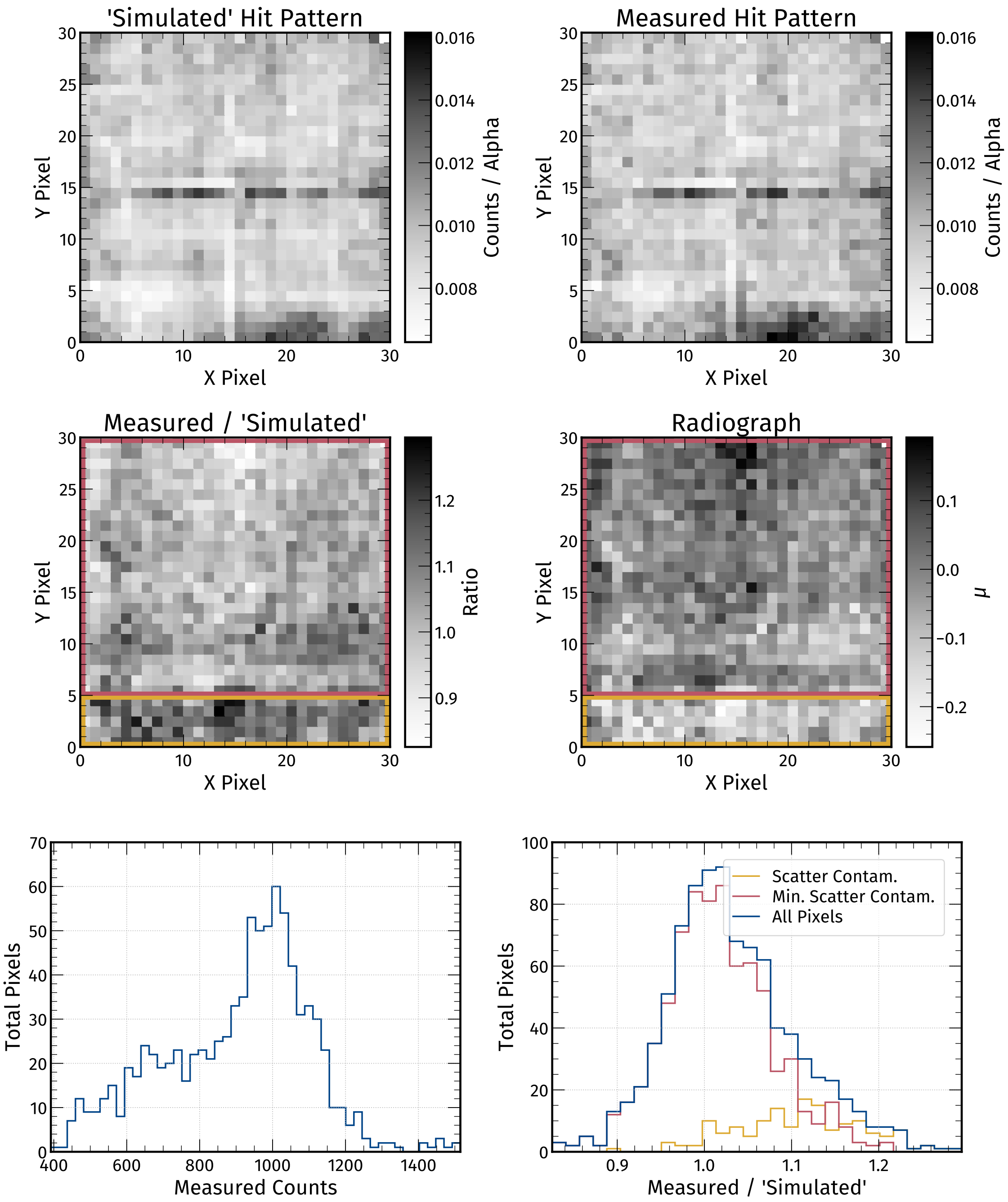

Figure 24. Final normalization from a void dataset. (*top left*) Calculated normalization. (*top right*): Measured void data. (*center left*): Ratio of measured void and calculated void-less normalization. (*center right*): Radiograph using measured void data and the calculated normalization. (*bottom left*) Distribution of total pixel counts for the measured void. (*lower right*): Distribution of measured/calculated pixel ratios. Orange and pink boxes and curves correspond to pixels within the pixel boundaries demarcated in the 2D ratio and radiograph plots.

As seen in Figure 24, the calculation does a good job of replicating the void measurement, with some noticeable differences. In particular, the bottom five rows of pixels are underpredicted in the normalization calculation, as shown in the ratio and radiograph plots (center row) and in the pixel ratio distribution histograms (lower right) in Figure 24. The origin of this discrepancy is under investigation, but it may arise from different amounts of material located near the panel in the two datasets. The neutrons likely directed slightly off the panel and scattering into the panel from material near the panel contributed different amounts to the calculated normalization and the measured void data. These events are close enough to the alpha-particle centroid and located near enough in time to the expected TOF of a 14.1 MeV neutron that they are not excluded in the analysis of measured data. The possibility of a scatter subtraction—as is typically performed when a void measurement is available—is under study, but the results are inconclusive at this time.

The bottom row of Figure 24 shows a histogram of the measured number of counts in the void dataset to enable comparison with the width of the ratio distribution (bottom right). Generally, the measured number of counts in each pixel are on the order of 1,000 events, resulting in expected statistical fluctuations of slightly more than 3% (producing expected fluctuations of roughly 4% in the ratio, assuming a normalization by a dataset with comparable statistics).

The bottom right panel of Figure 24 shows the distribution of the values from the ratio of the calculated to the measured void. Overlaid are the separated distributions from the bottom 5 rows (where the near-detector scatter effects are most noticeable) and from the remaining 25 rows of pixels. The mean ratio value of the bottom five rows of pixels is 1.11 ± 0.01 with a standard deviation of 0.07. The remaining pixels have an average ratio of 1.016 ± 0.002 with a standard deviation of 0.06, where the errors given are the statistical error on the mean. Note the Gaussian width of the normal pixel rows is roughly 2% larger than what would be expected from counting statistics, suggesting that some systematic uncertainty is unaccounted for.

4.4.2 Object Dataset

Data were also taken to test the voidless normalization calculation with an object consisting of a steel ring with a lead brick, as shown in Figure 25. This object was chosen to be large enough that multiple source–detector geometries were needed to form a complete image and thus provided a test dataset for gantryless image stitching (Section 5). The neutron panel was placed on a wheeled lift table to enable fast repositioning of the detector. Rough dimensions of the source–detector geometry were measured using a tape measure, but the final geometry information was inferred by the position-fitting algorithm discussed in Section 3. For the dataset with the panel nominally centered on the D-T spot, the panel front face was roughly 97.2 cm from the D-T source spot. The object was also nominally centered on the D-T spot, and the object center was roughly 59.8 cm from the spot. A single source–detector geometry (demarcated by the blue square in the left panel of Figure 25) was used to evaluate the voidless normalization performance.

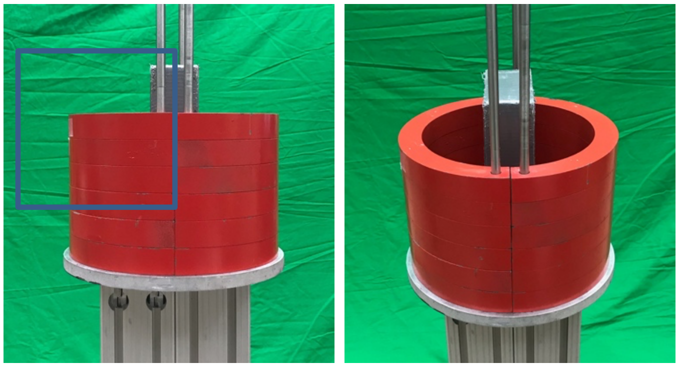

Figure 25. Object measurement to test voidless normalization calculation consisting of a steel ring and lead brick. Outlined in the blue square is the approximate location of the image in Figure 26.

The result of applying the voidless normalization is shown in Figure 26. The position used for the normalization calculation used the results from the position reconstruction detailed in Section 3. This test image was taken from the upper left of the ring-and-brick object to exhibit the full range of path lengths provided by this test object. The ring (particularly the edges) and brick are clearly visible in the ratio and radiograph images, and the area outside the object has a measured path length scattered about zero mean free paths as expected. The contamination from near-detector scatter in the bottom rows of pixels is less noticeable than in the void measurement shown in 4.4.1. This result may be due to a smaller amount of material directly under the neutron panel for this object measurement compared with the horizontal stage used for the void comparison.

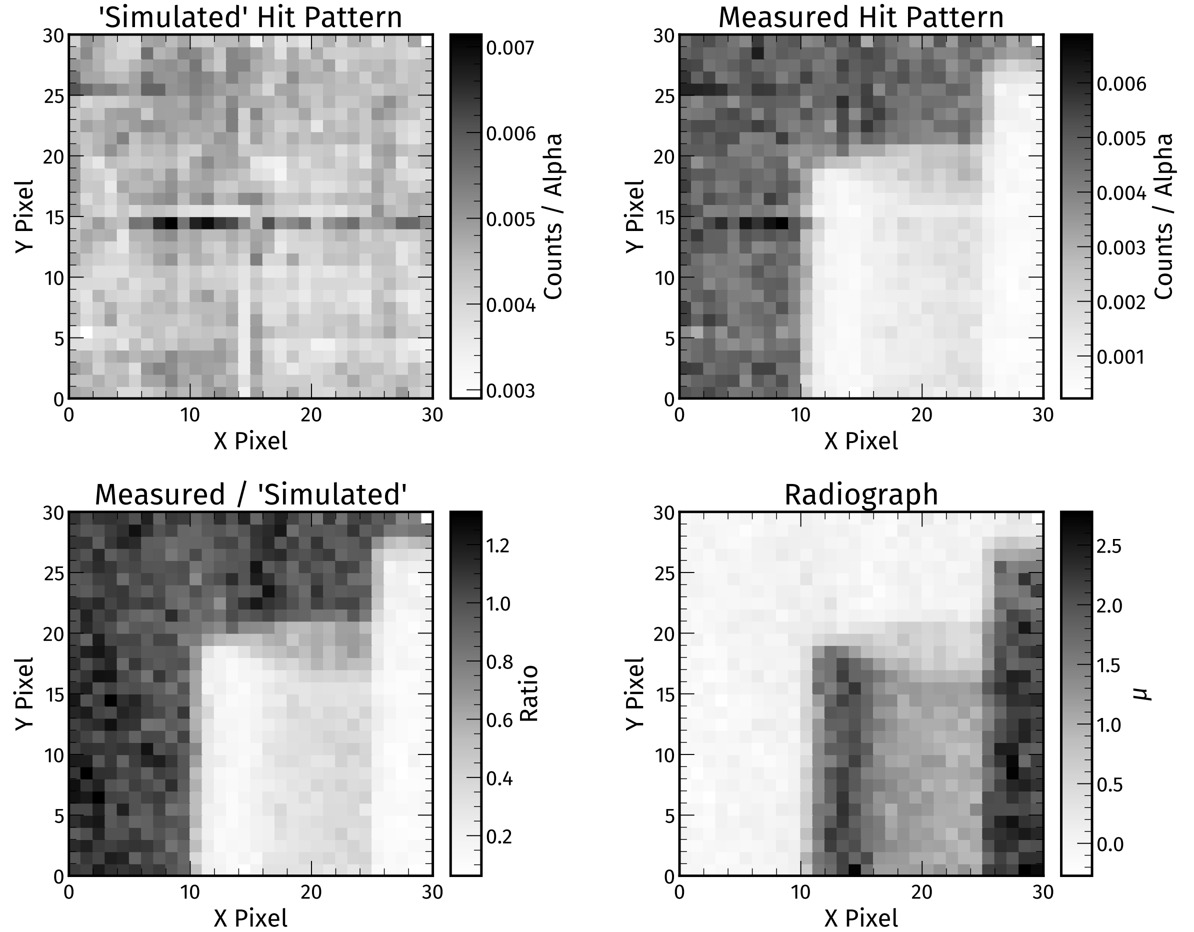

Figure 26. Final normalization from the steel ring and lead brick dataset. (*top left*) Calculated normalization. (*top right*) Measured data. (*center left*) Ratio of measured data and calculated voidless normalization. (*center right*) Radiograph using measured data and the calculated normalization. The left edge of the brick, top of the cylinder, and left edge of the cylinder are all visible in both the ratio and radiograph plots.

5. IMAGE STITCHING

The ability to produce a representative void measurement for a dataset, provided the location is known, allows for the creation of radiograph images using only the object measurement. However, some measurements may need to be recorded at multiple positions to completely cover the solid angle over which alpha-particle-tagged neutrons are incident on the object. Using the reconstructed positions from the detector panel localization routine, the individual radiographs may be combined into a composite image. An illustration of the neutron detector panel placed at three sequential positions in the neutron coincidence cone is shown in Figure 27. For maximum utility, the resultant images from each position in a series of measurements must be stitched into a composite image. For high-resolution x-ray images, feature matching is a common method for stitching images. However, feature matching is not readily applicable in the present situation because of the relatively small number of image pixels (900) and the potential for arbitrary positions and rotations of the neutron panel.

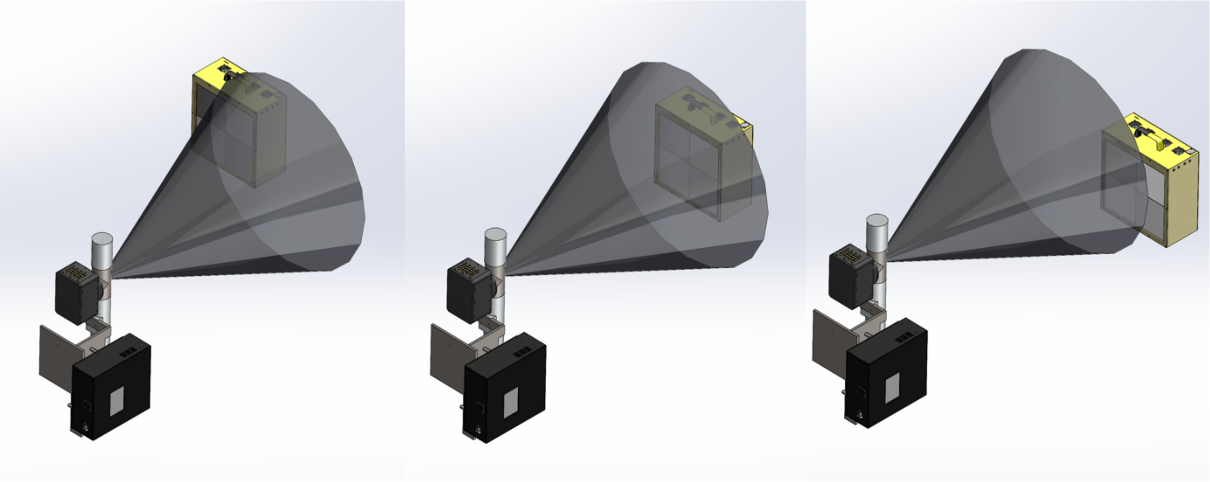

Figure 27. Illustration of three sequential neutron detector panel positions within the neutron coincident cone of the API D-T generator.

Instead, the individual radiographs are located in 3D space and projected onto a common image plane. For the sake of simplicity, this common image plane is defined as the *xy* plane at a distance z' from the source spot, which is the average reconstructed *z*-position for all images to be stitched. This image plane is then divided into pixels several times smaller than those of the neutron panel (the example image uses pixels one-fifth the size of the physical neutron pixels). These pixels are then populated by applying the following process to component radiographs:

1. Use the reconstructed position information to obtain vertex locations for all 900 radiograph pixels.

2. Project these vertices onto the image plane and assign the value of the radiograph pixel to all image pixels that lie within the polygon defined by the projected vertices.

3. Check for any image pixels that lie within the radiograph projection that did not inherit a value (this issue can arise because of the finite size of the image pixels). Assign those pixels the mean value of neighboring pixels.

The composite image is then formed by summing the projected images. The number of times that image pixels inherit a value from a parent radiograph is tracked so that regions where measurements overlap are properly normalized. Examples of a set of projected images are shown in Figure 28, and a merged composite for the object dataset is shown in Figure 29.

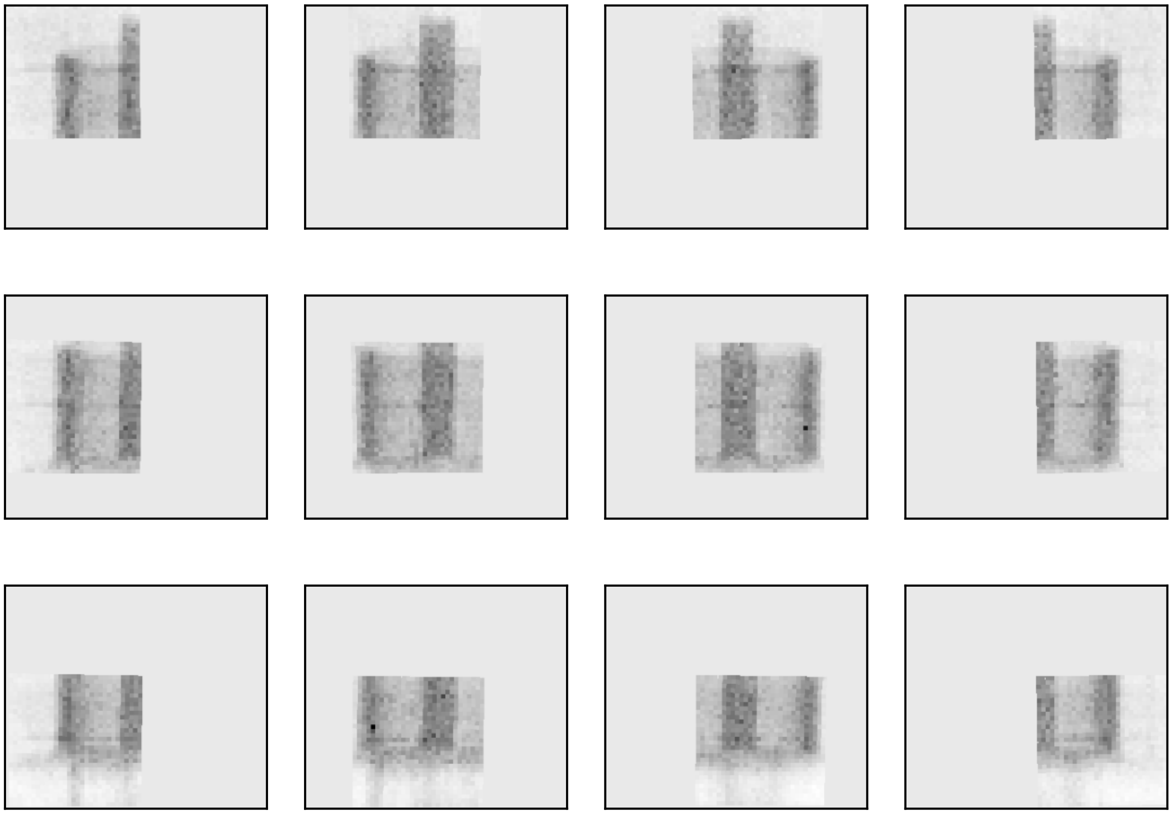

Figure 28. Set of radiographic images of the object in Figure 25 projected onto a common plane.

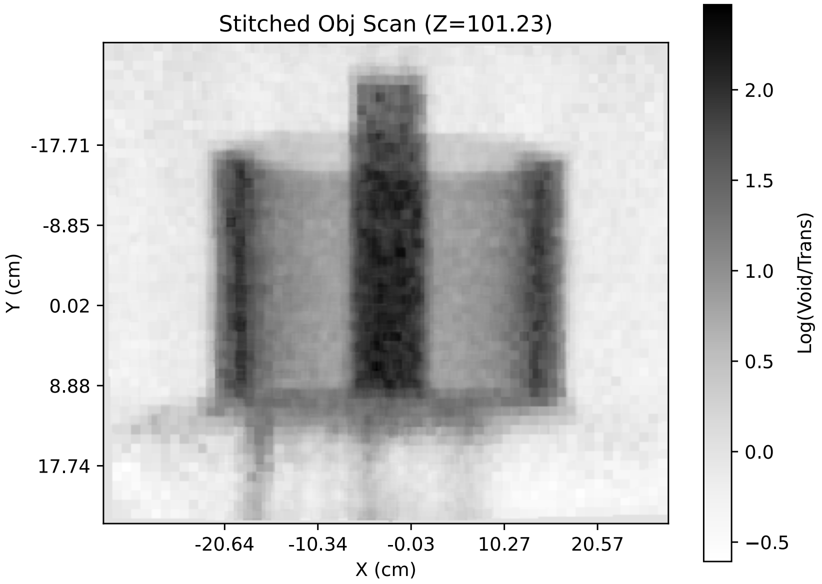

Figure 29. Composite radiograph formed by stitching multiple radiographic images.

6. SUMMARY/CONCLUSIONS

The present work developed and demonstrated an analysis chain to perform API neutron transmission radiography when (1) the source and detector panel are separately hand positioned rather than held in registration by a gantry, (2) multiple detector panel positions within the coincident cone of tagged neutrons are required to image an item of interest, and (3) it is not possible to obtain normalization measurements that have identical source–detector positioning but that do not include the inspected object .

The analysis depends on performing a robust characterization of the imaging system that requires alpha-particle/neutron coincidence data acquired for known detector positions that cover the neutrons' coincident cone. The initial part of the analysis chain determined detector calibrations. In particular, the characterization data are used to align all neutron and alpha-particle detector pixels so that measured time differences correspond to true TOFs, to determine direction vectors for each pixel of the alpha-particle detector, and to determine an efficiency map for all pixels of the neutron detector.

Then, for the calibrated imaging system, the detector position and orientation were determined from transmission data. To infer the detector position, first the position of each neutron pixel is inferred from the weighted average of coincident alpha-particle vectors and the summed TOF distribution. The position and orientation of the detector panel is determined from a best fit to the individual neutron pixel positions. The method is sensitive to movements of the panel of less than 0.5 mm, but the overall position accuracy ($\sqrt{\Delta x^2 + \Delta y^2 + \Delta z^2}$) is approximately 2.4 mm because of additional systematic errors; the sources of these systematic errors are being investigated to improve this localization to better than 0.5 mm.

Once the position of the detector is determined within the coincident neutron cone, an expected normalization or void can be calculated. The expected normalization uses the solid angle and efficiency of each pixel and its overlap with the coincidence cone of alpha-particle detector pixels. Discrepancies between the expected and measured normalizations are maximal near the bottom edge of the detector panel and are presumably caused by in-scattering from surfaces on which the detector rests. A radiograph is determined as the negative logarithm of the ratio of measured counts to expected normalization counts.

The inferred detector positions also enable projection of multiple radiographs into a common plane to form a stitched image. Despite the relatively low detector panel spatial resolution, accurate stitching can be performed without requiring overlapping neutron detector panel locations.

7. REFERENCES

[1] P. Hausladen, M. Blackston, J. Mullens, S. McConchie, J. Mihalczo, P. Bingham, M. Ericson, L. Fabris, 2010, "Induced-Fission Imaging of Nuclear Material," Available: https://www.osti.gov/biblio/983561, Accessed November 3, 2022.

[2] M. A. Blackston and P. A. Hausladen, 2015, "Fast-neutron elastic-scatter imaging for material characterization," *2015 IEEE Nuclear Science Symposium and Medical Imaging Conference (NSS/MIC)*, pp. 1–9. https://doi.org/10.1109/NSSMIC.2015.7581846.

[3] M. Blackston, P. Hausladen, and J. Gregor, 2019, *Progress Update on Iterative Reconstruction of Neutron Tomographic Images, 2019*, ORNL/SPR-2019/1353, Oak Ridge, Tennessee: Oak Ridge National Laboratory,. https://doi.org/10.2172/1615803.

[4] P. A. Hausladen, M. A. Blackston, A. J. Gilbert, J. Gregor, J. K. Mattingly, 2021, *Progress on Associated-Particle Imaging Algorithms, 2021*, ORNL/SPR-2021/2253, Oak Ridge, Tennessee: Oak Ridge National Laboratory.

[5] D. L. Chichester, M. Lemchak, and J. D. Simpson, 2005, "The API 120: A portable neutron generator for the associated particle technique," *Nucl. Instrum. Methods Phys. Res. Sect. B Beam Interact. Mater. At.* 241 (1): 753–758, https://doi.org/10.1016/j.nimb.2005.07.128.

[6] M. R. Heath et al., 2022, "Development of a Portable Pixelated Fast-Neutron Imaging Panel," *IEEE Trans. Nucl. Sci.* 69 (6): 1352–1356, https://doi.org/10.1109/TNS.2021.3136344.

[7] S. Das, 2016, *A simple alternative to the Crystal Ball function*. Available: https://arxiv.org/abs/1603.08591, Accessed November 3, 2022, https://doi.org/10.48550/arXiv.1603.08591.

[8] Detwiler, J., N. Sebe, 2021, "legend-exp/g4simple: A simple Geant4 simulation suite," Available: https//github.com/legend-exp/g4simple, Accessed: September 1, 2022.

[9] S. Agostinelli et al., 2003, "GEANT4–a simulation toolkit," *Nucl Instrum Meth A*, 506 (3): 250–303, https://doi.org/10.1016/S0168-9002(03)01368-8.

[10] J. Allison et al., 2006, "Geant4 developments and applications," *IEEE Trans Nucl Sci* 53 (1): 270, https://doi.org/10.1109/TNS.2006.869826.

[11] J. Allison et al., 2016, "Recent developments in Geant4," *Nucl Instrum Meth A* 835: 186–225, https://doi.org/10.1016/j.nima.2016.06.125.